

Fishing Bans in Chinese Waters: Effectiveness and Spillovers

Haishan Yuan*

University of Queensland

February 21, 2025

Abstract

China's large-scale seasonal fishing bans aim to promote sustainable fisheries, yet their effectiveness remains uncertain given the challenges of monitoring vast ocean areas. Using a novel dataset of nighttime vessel detections and a regression discontinuity in time (RDiT) design, we find that the bans reduce boat detections within China's Exclusive Economic Zone (EEZ) by 72%, with a sharp increase upon lifting. Boat detections also decline in neighboring EEZs at the start of China's bans, indicating regulatory spillovers. Data from AIS-equipped vessels reveal that Chinese boats operate in neighboring EEZs, while foreign vessels fish in the Chinese EEZ. Compliance weakens in the later stages of the bans, with more boats detected in areas with favorable conditions. My findings suggest that command-and-control approaches can be effective for fishery management in contexts where market-based alternatives may not be practical. The results also underscore the importance of addressing regulatory spillovers and strengthening complementary enforcement.

Keywords: Tragedy of the Commons; Regression Discontinuity in Time or Space; Fishing Ban; Fishery; Exclusive Economic Zone (EEZ); EEZ Incursion; Regulatory Spillover.

JEL Classification Numbers: Q22, Q56, Q58, K42, O13

* Address: Level 6, Colin Clark Building (39), University of Queensland, St Lucia, QLD 4072, Australia; Email: h.yuan@uq.edu.au; I thank the editor, two anonymous referees, Hee-Seung Yang, Youjin Hahn, Alberto Posso, and the participants at the KDI-3ie Conference on Impact Evaluation in Development Research, Monash Environmental Economics Workshop, Australasian Development Economics Workshop, and ADEA-QUT Conference for their helpful comments. This paper was previously circulated as "Fishing Ban." All errors are mine. Disclosure: I do not have significant competing financial, professional, or personal interests that might have influenced the work described in this manuscript.

1 Introduction

Fisheries and aquaculture provide livelihoods for 10-12 percent of the world's population ([U.N. Food and Agriculture Organization, 2014](#)).¹ In 2014, the sector directly employed 38 million people, with 80 percent of motorized fishing vessels concentrated in Asia ([U.N. Food and Agriculture Organization, 2016](#)). China, which maintains the world's largest fishing workforce and fleet, employed 5.75 million fishery workers in 2015, including 3 million traditional fishermen ([China Fishery Statistical Year Book, 2016](#)).²

Despite the economic importance of the sector, the FAO estimates that 31.4 percent of world fish stocks in 2013 were fished at biologically unsustainable levels. An additional 58.1 percent of stocks were fully exploited, leaving only 10.5 percent under-exploited ([U.N. Food and Agriculture Organization, 2016](#)). This widespread overexploitation represents a classic example of the tragedy of the commons, where Coasian solutions are infeasible and government intervention becomes necessary. In response, China has implemented the world's first large-scale seasonal fishing bans, prohibiting commercial fishing in its Exclusive Economic Zone (EEZ) for two to four months each summer. However, given the challenges of ocean surveillance and the typical difficulties in measuring illicit activities, direct evidence on the effectiveness of such fishing regulations remains limited. This paper addresses this gap using novel nighttime satellite imagery data on offshore vessel detection from the new-generation weather satellite program.

Using a regression discontinuity in time (RDiT) design, I estimate that the implementation of fishing bans reduces nighttime boat detections by 73 percent, while the subsequent lifting of bans reverses this decline. I also obtained position data from AIS-equipped vessels, which tend to be larger and account for approximately 86 percent of Chinese vessels 12 meters or longer. Applying a similar RDiT design, I find comparable reductions in the number of vessels operating within China's EEZ at the onset of fishing bans, with an even larger decrease in total fishing hours. Likewise, there are sharp increases in vessel counts and fishing hours following the lifting of fishing bans.

The enforcement of the fishing bans is by-and-large effective but far from perfect.

¹Throughout this paper, I use data from the Food and Agriculture Organization (FAO) of the United Nations' State of World Fisheries and Aquaculture reports, which are considered the authoritative source on global fishing statistics.

²In 2015, 20 percent of Chinese fishery workers were women. Throughout this paper, "fishermen" refer to both men and women in the fishery sector.

Although the start of bans leads to substantial reductions in boat detections and fishing hours, considerable fishing activity persists, as evidenced by nighttime satellite imagery and AIS position data. There is also evidence of increased fishing ban violations later in the ban periods, with both boat counts and fishing efforts gradually rising as the bans progress. Furthermore, areas predicted to be productive for fishing, based on oceanographic variables, show higher boat presence in the later stages of the bans. The difference-in-differences estimates are smaller than the RDiT estimates, suggesting that the local average treatment effects at the onset of fishing bans may be higher than the average treatment effects over a more extended period.

Furthermore, I find no evidence of spatial discontinuity at the Exclusive Economic Zone (EEZ) border during the fishing ban, suggesting imperfect enforcement of territorial fishing rights. Moreover, I find substantial spillover effects of the Chinese fishing bans in neighboring EEZs. The starts of the Chinese fishing bans also reduce the boat detections in bordering EEZs. Similarly, but to a less extent, the lifting of the Chinese fishing bans increase the boat detections in the neighboring water. While the spillovers are unlikely to be driven by larger vessels equipped with AIS devices that broadcast their positions, my findings suggest that the impacts of Chinese fishing bans are not limited to the Chinese EEZs.

This paper contributes to a large literature on the policies for the conservation of the environment and natural resources (see [Cropper and Oates, 1992](#) and [Brown, 2000](#) for a review). To the best of my knowledge, this paper is the first to empirically investigate the effectiveness of the Chinese summer fishing ban, which is the first large-scale regulatory policy for a sustainable fishery in a developing country or in the form of seasonal, complete ban on commercial fishing.³

The literature on environmental conservation policies has found that subnational inter-jurisdictional spillovers are important in considering a national policy on environmental conservation (see, e.g., [Burgess et al., 2012](#); [Lipscomb and Mobarak, 2016](#)). The literature also documents important spillovers of environmental regulation (and enforcement thereof) across firms ([Chan and Zhou, 2021](#)), and the relocation of economic activities due to environmental regulation ([Walker, 2011](#); [Carruthers and Lamoreaux, 2016](#)).

My findings suggest that, in the context of the sustainable marine fishery, interna-

³In parallel, unpublished work, [Bos \(2021\)](#) also investigates the Chinese fishing ban using VIIRS VBD and AIS-based data. He similarly finds that the Chinese fishing bans are effective but not perfectly enforced. However, this paper differs in several respects, including the use of RDiT as an empirical approach and the investigation of spatial discontinuities at the EEZ borders.

tional spillover in regulatory policy also affects the effectiveness of environmental regulation. My findings echoes with what [Sigman \(2002\)](#) called international free-riding in regulating pollution of transnational river systems.

This paper also contributes to the growing literature that uses remote sensing data to measure and study environmental conditions and economic activities (see, e.g., [Henderson et al., 2012](#); [Michalopoulos and Papaioannou, 2013](#); [Hodler and Raschky, 2014](#); [Lipscomb and Mobarak, 2016](#); [Chan and Zhou, 2023](#), and [Donaldson and Storeygard, 2016](#) for a review). In particular, [Assunção et al. \(2023\)](#) studied the use of a remote sensing system to monitor and enforce conservation efforts in the Brazilian Amazon, where illegal logging was widespread due to weak institutional protection for the environment. They found that the remote sensing system in Brazil greatly facilitated effective environmental monitoring and regulation enforcement against deforestation. Given that the implementation and enforcement of environmental regulations critically depend on monitoring and measurements ([Lipscomb and Mobarak, 2016](#); [He et al., 2020](#)), the findings in this paper highlight the promising potential of using remote sensing data for enforcing environmental regulations.

[Flückiger and Ludwig \(2015\)](#) and [Axbard \(2016\)](#) found that negative income shocks from fishery increase piracy, which induced violence and substantial welfare losses, including by interrupting shipping routes ([Besley et al., 2015](#)). In light of these studies, my findings suggest that fishing bans may have both short-run and long-run effects on piracy across regions.

The remainder of the paper proceeds as follows. Section 2 provides institutional background on seasonal fishing ban policies. Section 3 describes the data, leaving details to Appendix B. Section 4 presents evidence on the effectiveness of Chinese fishing bans. Section 5 examines the compliance during fishing bans. Section 6 documents evidence of regulatory spillovers and discusses issues of displacement. Section 7 investigates the activities of foreign fleets in Chinese waters. Section 8 concludes.

2 Background

2.1 Fishing Ban: Why?

China's marine fishing industry has surged since market reforms in the late 1970s. By 2016, China boasted the world's largest fishing workforce and fleet, with 20 million people reliant on fisheries and 14 million directly or indirectly employed in the

sector ([China Fishery Statistical Year Book, 2016](#)). The fishing fleet exceeded one million vessels, two-thirds of which were motorized. As shown in Table 1, of the 272,000 motorized vessels operating at sea, 69% were small-scale, under 12 meters long.

Despite the growth in catches, fish stocks declined rapidly ([Watson and Pauly, 2001](#)). Early management policies in the 1980s and 1990s proved inadequate. From the mid-1990s, China implemented seasonal fishing bans and policies to reduce fishing capacity.

Table 1: Number of Seafaring Fishing Vessels by Size

	Number		Tonnage	
Less than 12 meter	186,781	68.6%	882,361	10.0%
12 meter to 24 meter	49,697	18.2%	1,919,347	21.8%
24 meter or longer	35,844	13.2%	5,989,801	68.1%
Total	272,322	100%	8,791,509	100%

Notes: Data as of the end of 2015 from the [China Fishery Statistical Year Book \(2016\)](#).

2.2 Fishing Ban: When and Where?

China's first seasonal fishing ban was imposed in the Yellow Sea and East China Sea in 1995, extending to the South China Sea by 1999. The bans prohibit commercial fishing in China's Exclusive Economic Zone (EEZ) for 2 to 4 months annually. As shown in Table 2, ban durations vary by marine area and have been extended in recent years. Figure A.1 maps these regulatory zones and their neighboring EEZs.

2.3 Fishing Ban: How?

The vastness of the ocean poses significant challenges to the effective enforcement of fishing bans. During ban periods, the China Coast Guard, in coordination with provincial fisheries ministries, undertakes patrols and inspections of fishing vessels to ensure compliance. Violations of these bans are subject to prosecution. For example, in 2017, Chinese authorities conducted patrols spanning over 800,000 nautical miles, inspected approximately 76,000 fishing vessels, issued fines for 2,764 fishing ban violations (including over 100 criminal prosecutions), and confiscated 800 tons of fish along with 89,000 meters of fishing nets ([Ministry of Agriculture, 2017](#)).

Table 2: Effective Dates of Fishing Bans

Zone	Years 2009 – 2016		Year 2017 onward	
	Start	End	Start	End
1 Northern Yellow Sea	June 1	Sep. 1	May 1	Sep. 1
2 Southern Yellow Sea & Northern East China Sea	June 1	Sep. 16	May 1	Sep. 16
3 Southern East China Sea	May 16	Aug. 1	May 1	Aug. 16
4 Taiwan Strait & South China Sea	May 16	Aug. 1	May 1	Aug. 16

Notes: This table lists the start and end dates of fishing bans in each zone for different years. Zones are shown in Appendix Figure A.1. Minor exceptions applied to certain fishing methods in Zones 2 and 3.

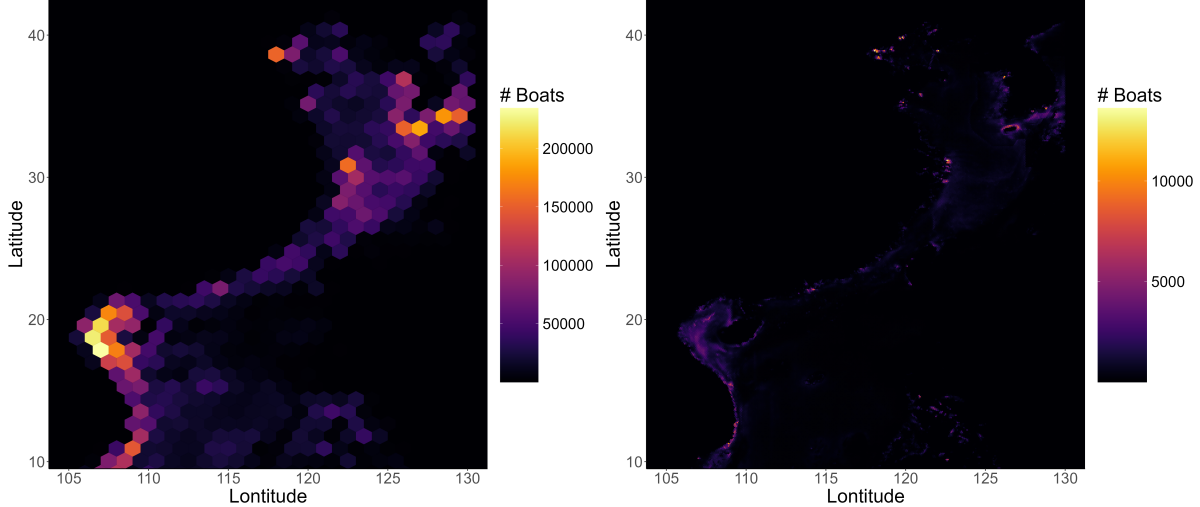
To regulate fishing capacity, China adopted a zero-growth policy in 1999, accompanied by a strict vessel licensing policy. During fishing ban periods, fishery authorities inspect ports to identify unregistered vessels and detect fishing ban violations among both registered and unregistered vessels. In certain regions, fishermen are also required to surrender their fishing equipment during the ban period. To offset income losses during these bans, the Chinese government has recently introduced modest subsidies for fishermen.

3 Data Description

3.1 VIIRS Boat Detection Data

The primary dataset is the VIIRS Boat Detection (VBD) data, which provides nighttime vessel detections using remote sensing imagery from the Suomi National Polar-orbiting Partnership satellite. This dataset offers high spatial resolution and sensitivity, making it well-suited for detecting fishing activity. The VBD data in my sample span April 2, 2012, to December 31, 2017, capturing strong and weak boat detections while excluding blurry detections, gas flares, glows, recurring lights, and offshore platforms. Detailed information on the VBD data, including its technical specifications and processing algorithms, is provided in Appendix B.

Figure 1: Boats at Night



Notes: Each hexagonal cell in the heatmap represents total boat detections during the sample period. The left subplot uses 1-degree hexagons (~ 100 km), while the right uses 0.1-degree hexagons (~ 10 km), with latitude (N) and longitude (E) defining the axes.

Figure 1 shows the spatial density of boat detections in China’s EEZ and adjacent waters. The left panel, at 1-degree resolution ($7,100 \text{ km}^2$), reveals up to 200,000 detections per cell (28 per km^2 over 4.75 years), with higher densities near coastal cities like Shanghai and Guangzhou. The right panel, at 0.1-degree resolution (71 km^2), shows up to 10,000 detections per cell (140 per km^2), with bright spots near the Shandong and Liaodong Peninsulas.

Coastal areas exhibit higher densities, consistent with AIS-based studies (Yan et al., 2022). Outside China’s EEZ, significant activity near Jeju Island (South Korea) and Vietnam’s coast reflects overfishing pressures. The figure highlights substantial spatial variation, with key regions serving as primary fishing grounds.

3.2 Cloud Cover & Oceanographic Conditions

Cloud cover affects satellite detection of nighttime light and boats, so I incorporate it to improve boat detection accuracy. Using VIIRS cloud mask data (500m resolution) from the Earth Observation Group, I identify and aggregate cloud-covered pixels within regulatory zones in China’s EEZ to calculate the nightly proportion of cloud-covered pixels.

Oceanographic conditions, such as chlorophyll-a concentration and sea surface temperature, affect marine fishing productivity (Flückiger and Ludwig, 2015; Axbard, 2016). I obtained chlorophyll-a (a proxy for phytoplankton abundance) and sea sur-

face temperature data from NASA’s Ocean Color platform. Both datasets are derived from VIIRS imagery and have a 9 km resolution and daily frequency, offering insights into marine biological productivity.

3.3 AIS-based Measures of Fishing Activities

To measure fishing effort, Global Fishing Watch (GFW) uses Automatic Identification System (AIS) data, a vessel tracking system originally designed for collision avoidance. Machine learning models, including convolutional neural networks (CNNs), classify fishing vessels and detect fishing activities by analyzing billions of AIS positions ([Kroodsma et al., 2018](#)). AIS broadcasts a vessel’s identity, position, speed, and turning angle, enabling the identification of fishing behaviors, such as the slower speeds typical of trawlers during fishing ([Yan et al., 2022](#)).

The GFW dataset, spanning 2012–2020, tracks over 100,000 unique fishing vessels, with approximately 70,000 active annually. It provides vessel-level data on fishing hours and vessel presence at a spatial resolution of 0.1 degrees. This dataset allows for the aggregation of fishing effort by regulatory zones and the analysis of fishing activities by vessel registration country.

A limitation of AIS data is that devices can be disabled to evade monitoring, particularly during illegal fishing. To address this, [Welch et al. \(2022\)](#) developed a rule-based model to identify AIS-disabling events, revealing over 55,000 suspected cases between 2017 and 2019. These events, obtained from GFW, provide insights into gaps in AIS coverage and potential illegal fishing activities.

4 Effectiveness of Fishing Bans

This section employs two empirical approaches to evaluate the impact of China’s summer fishing bans on boat detections in Chinese Exclusive Economic Zones (EEZs). The first approach is a regression discontinuity in time (RDiT) design (see [Hausman and Rapson, 2018](#)). The second approach is a difference-in-differences design.

4.1 Parametric Estimation with RDiT Design

The RDiT design leverages time-series variation in fishing ban policies across regulatory zones. To implement the RDiT design parametrically and nonparametrically,

I first aggregate nightly boat detections within each regulatory zone, as shown in Figure 1 and detailed in Table 2.

The parametric approach accounts for seasonal variations using a polynomial specification and estimates the effects of fishing bans with a binary treatment indicator. Specifically, I estimate:

$$Y_{zt} = \gamma B_{zt} + f(t) + \delta' X_{zt} + \epsilon_{zt} \quad (1)$$

where Y_{zt} is the log number of boat detections in zone z on night t ; B_{zt} indicates whether a fishing ban is effective; $f(t)$ is a polynomial in day of year (1-366); X_{zt} is a vector of controls; and ϵ_{zt} is the error term.

Table 3 presents estimates of γ . Columns (1) and (2) focus on the onset of fishing bans, excluding post-ban observations, while Columns (3) and (4) examine the lifting of bans, excluding pre-ban observations. For consistency and brevity, I use a single treatment indicator that equals one during active bans across all specifications, rather than separate indicators for ban implementation and lifting.

Table 3: Fishing Ban and the Number of Boats Detected: RDiT Estimates

	Ban ON		Ban OFF	
	(1)	(2)	(3)	(4)
Fishing Ban Effective	-0.911*** (0.162)	-0.644*** (0.113)	-0.687*** (0.133)	-0.451*** (0.111)
Obs.	4791	4791	5053	5053
Sample	Days before a fishing ban's lifting		Days after a fishing ban becoming effective	
Day of the Week F.E.	-	X	-	X
Day of the Lunar Month F.E.	-	X	-	X
Share of Cloudy Pixels	-	X	-	X

Notes: This table reports the parametric estimates of fish ban on the log number of boat detections. All specifications include a quadratic term of the day of the year to control for seasonal effects, and a zone fixed effect. The specifications in Columns (2) and (4) additionally include day of the week indicators, day of the lunar month indicators, and the share of cloudy pixels in a regulatory zone in a night. Columns (1) and (2) exploit the discontinuity in time when fishing bans become effective, and therefore drop observations after the fishing bans were lifted in the later part of the year. Columns (3) and (4) exploit the discontinuity in time when fishing bans were lifted by dropping the observations before the fishing bans became effective in the early part of the year. In all columns, "Fishing Ban Effective" is a binary variable that equals one if a fishing ban is in effect on that day and zero otherwise. [Newey and West \(1986\)](#) heteroskedasticity-and-autocorrelation robust standard errors are reported in the parentheses, where the maximum lag of serial correlation is 35 nights. * $p < 0.10$; ** $p < 0.05$; *** $p < 0.01$.

All specifications include a quadratic time polynomial to capture seasonal patterns, and a zone fixed effect (F.E.). Columns (2) and (4) additionally control for cloud cover, day-of-week, and lunar day-of-month fixed effects. These controls address systematic variations in fishing activity due to work schedules and measurement challenges, such as cloud cover and lunar reflections affecting satellite detection. Standard errors, reported in parentheses, are robust to heteroskedasticity and autocorrelation, following [Newey and West \(1986\)](#), with serial correlation allowed up to 35 nights.

The results indicate that the start of fishing bans has large, negative, and statistically significant effects on boat detections at the 1% level. Specifically, the onset of fishing bans reduces boat detections by 47% to 60%. Conversely, the lifting of bans has similarly large, positive effects, reversing the reductions observed during the bans.

In Appendix Table A.1, I estimate the specification in Eq. (1) by regulatory zone. The by-zone estimates show that summer fishing bans significantly reduce boat detections, with effects varying by zone. Zones 1 and 4 exhibit the largest and most consistent reductions (51 to 108 log points, significant at 1%), while Zone 2 shows the largest initial reductions (100 to 128 log points) but no significant effects when bans are lifted. Zone 3 also shows consistent reductions during implementation (30 to 88 log points), though effects diminish after bans are lifted.

Overall, the start of fishing bans reduces boat detections by 50% to 72%, with the strongest impacts during implementation. The lifting of bans has more muted and variable effects, ranging from no impact in Zone 2 to increases of up to 225% in other zones. These results highlight the substantial and zone-specific impacts of fishing bans.

4.2 Graphic Representation and Non-parametric Estimation of RDiT

To complement the parametric analysis, I employ a nonparametric RD in Time design examining transitions at ban implementation and lifting. The identification assumes smooth time trends in the absence of treatment. For each regulatory zone and year (2012-2017), I normalize the first night after ban implementation/lifting to zero, with the running variable defined as nights before/after these transitions within a [-50, 50] window.

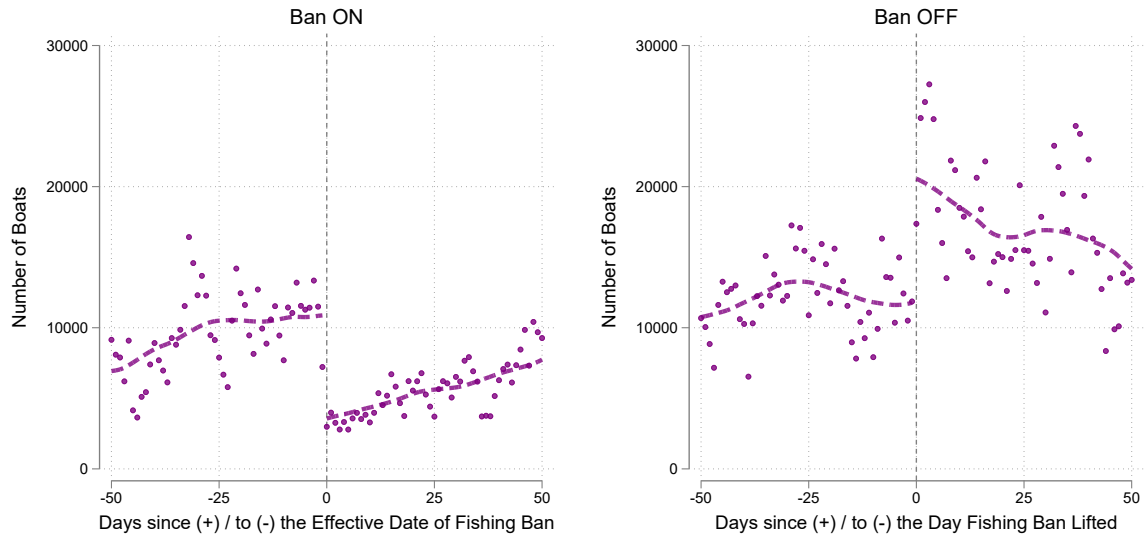
Figure 2 reveals sharp discontinuities at both transitions. When bans take effect, boat detections drop from approximately 11,000 to 4,000 in the first night, with no evidence of anticipatory fishing intensification before implementation.

When bans are lifted, detections surge from 12,000 to 25,000 within two nights, fol-

lowed by a gradual decline as fish stocks are depleted. The observed pattern of vessels returning to harbor approximately one day before the ban starts is consistent with the time needed for vessels to return from distant fishing grounds, given typical cruising speeds and EEZ boundaries up to 370 km offshore.

Formal nonparametric regression discontinuity (RD) estimates confirm these visual patterns (Appendix Table A.2). Ban implementation reduces boat detections by 8,224 per night (88% decrease), while lifting increases detections by 10,701 (86% increase). Calonico et al. (2014) estimates are highly statistically significant and robust to randomization inference tests reported in Appendix Figure A.2, though the lifting effects show somewhat less precision than implementation effects.

Figure 2: Boat Detected at Night around the Imposition and Lifting of Fishing Bans



Notes: This figure shows two RD plots examining nighttime boat detections around China's seasonal fishing ban transitions during 2012-2017. The left plot shows changes when bans begin ("Ban ON"), while the right plot shows changes when bans end ("Ban OFF"). Each point represents the total number of boats detected across all regulatory zones, aggregated by nights before/after ban transitions. Day 0 marks the first night following the transition, as bans begin/end at noon. The x-axis spans 50 nights before and after transitions. Dashed lines represent local polynomial fits on each side of the cutoff. The sample includes four regulatory zones in Chinese waters where seasonal fishing bans were implemented.

To examine potential heterogeneity across regulatory regions, Appendix Figure A.3 presents separate RD plots for each zone. Zone-specific analyses show that the sharp discontinuities in boat detections at ban implementation and lifting are consistent across all regulatory zones. Parametric and nonparametric RD estimates (Appendix Tables A.1 and A.2) confirm statistically significant effects in most zones, with reductions of 62-93% at implementation and increases of 19-149% at lifting. Despite modest

regional variations, the overall pattern of sharp declines at implementation and rapid increases at lifting remains consistent across all zones, supporting the robustness of the aggregate findings.

To complement the satellite detection data, I analyze vessel counts from GFW's AIS data, matching 0.1-degree cells to Chinese EEZ regulatory zones. While this dataset primarily captures larger vessels equipped with AIS transmitters, it provides a useful comparison to the satellite detections and offers information about vessels' flag states.

Fishing vessels at least 12 meters long account for 90% of the tonnage of fishing vessels in China ([China Fishery Statistical Year Book, 2016](#)). A significant portion of these larger vessels are equipped with AIS. Because larger vessels are more powerful and have greater fishing capacity, a considerable portion of the global fish catch likely comes from vessels equipped with AIS. Furthermore, the fishing vessels recorded in the fishing effort dataset represent approximately 86% of registered fishing vessels at least 12 meters long in China in 2014.

As shown in Figure A.4, which presents aggregate patterns across all four regulatory zones, and Figure A.5, which breaks down the analysis by individual zones, the RD analysis of AIS data reveals patterns similar to those found in satellite detections, with even sharper discontinuities at ban transitions in each zone. This heightened clarity may reflect both the weather-independence of AIS signals and potentially stricter enforcement for larger, more easily identifiable vessels. The data also confirms the pre-ban decline in vessel activity observed in satellite data, suggesting systematic return-to-port behavior.

4.3 Validity and Robustness of the RDiT Design

The validity of my RD design relies on the assumption that potential confounders change smoothly at the treatment threshold. I test this assumption by examining two key oceanographic variables that could affect fishing activities: chlorophyll-a concentration and sea surface temperature. Using NASA Ocean Color VIIRS data at 9 km × 9 km spatial resolution, I test for discontinuities in these variables around ban transitions. Figure A.6 shows no significant jumps in either variable at ban implementation or lifting, with formal tests confirming the absence of discontinuities.

Another potential concern is temporal displacement of fishing activities around ban transitions. Since ban dates are announced in advance, fishermen might intensify fishing just before implementation or adjust their return timing. On the other hand, the

data shows that vessels systematically return to port approximately one day before ban implementation, which could bias the RD estimates since this predictable fleet movement affects boat detections right around the cutoff. To address these concerns, I implement a donut hole RD design following [Barreca et al. \(2011\)](#), excluding observations within a 7-day window around transitions. This approach helps address potential biases from both return-to-port behavior and any pre-ban fishing intensification. Results (Appendix Table A.3) remain qualitatively similar to my main estimates, with slightly larger magnitudes.

While fishing vessels might be expected to intensify their activities before bans begin and stockpile frozen seafood for sale during ban periods, Figures 2 and A.4 show no evidence of such short-term temporal displacement. This absence of pre-ban intensification aligns with institutional features of Chinese fisheries. The dominance of fresh seafood in Chinese consumption patterns, combined with competition from aquaculture, limits incentives for pre-ban fishing intensification. Moreover, seasonal biological constraints and high operational costs (fuel and ice comprising 20.1% of costs according to [Ministry of Agriculture and Rural Affairs \(2019\)](#)) make substantial short-term shifting of fishing activity unprofitable. However, as discussed in Section 6, fishing households may compensate for lost income during bans by redistributing their fishing activities throughout the non-ban period.

4.4 Difference-in-Differences Estimation

While RD designs provide estimates of local average treatment effects (LATEs) around the threshold, these estimates may differ from the average treatment effects (ATEs) over the entire ban period, even in the absence of intertemporal displacement in fishing activity. This divergence could arise from several factors, including seasonal variation in fishing productivity and potential demand accumulation for fresh seafood during prolonged bans, both of which may affect ban enforcement. From a policy perspective focused on sustainable fishery management, understanding both the ATE during the ban period and the optimal ban duration is crucial. To shed light on these issues, I implement a difference-in-differences design that exploits a 2017 policy change in ban timing.

Prior to 2017, fishing bans began on June 1st for Zones 1 and 2, and on May 16th for Zones 3 and 4. Starting in 2017, all zones implemented a uniform ban start date of May 1st. The left panel of Figure A.7 normalizes time relative to May 1st (day zero)

and displays the average number of detected boats by year. Post-2017 observations, represented by solid diamonds, show an expected drop at time zero. In contrast, pre-2017 observations, shown by hollow circles, exhibit no comparable decline on May 1st. This placebo test, leveraging the historical variation in start dates, corroborates that the post-2017 reduction in detected vessels is attributable to ban implementation.

The right panel of Figure A.7 presents a similar placebo test examining the extension of fishing bans in Zones 3 and 4. Before 2017, these zones lifted their bans on August 1st; since 2017, the ending date has shifted to August 16th. Normalizing time relative to August 16th (day zero), the figure plots average boat detections before and after 2017. Post-2017 data, marked by solid yellow diamonds, reveal a sharp increase in detected vessels at day zero. Pre-2017 data, indicated by hollow blue circles, show no comparable discontinuity. This placebo test using the shifted ban ending date further confirms the causal effect of ban termination on vessel activity.

Figure A.7 motivates a difference-in-differences strategy that uses observations from different years but identical calendar dates within zones as controls, thereby accounting for zone-specific seasonality in vessel detection. I implement this strategy using three specifications, with results reported in Table 4. The unit of observation is an EEZ-day, with each regulatory zone in Chinese waters treated as a separate EEZ. While most coastal nations possess a single EEZ, some countries, such as the United States, maintain multiple EEZs (e.g., around Alaska, Hawaii, and along the eastern seaboard). The dependent variable in all specifications is the log number of detected vessels.

Column (1) includes year fixed effects and EEZ-specific month effects. Column (2) incorporates both EEZ-specific year effects and EEZ-specific month fixed effects. Column (3) employs EEZ-specific year fixed effects and EEZ-specific calendar day fixed effects. The key independent variable is a binary indicator for an active fishing ban, which takes a value of one only for the relevant Chinese EEZ zone during ban periods. Identification stems from within-zone variation in ban effective dates across years.

Standard errors are calculated using two approaches. Two-way cluster-robust standard errors, reported in parentheses, allow for arbitrary correlation within an EEZ across dates and within a date across EEZs. Conley (1999) spatial-temporal robust standard errors, reported in brackets, account for spatial correlation up to 1,000 kilometers and temporal correlation up to 35 nights.

The coefficients are statistically significant at the 5% or 1% level across both standard error calculations, with the exception of Column (1)'s estimate, which achieves

Table 4: Difference-in-Differences Estimates of Fishing Ban on Boat Detections

	(1)	(2)	(3)
Fishing Ban Effective	-0.272 (0.139)* [0.111]**	-0.311 (0.139)** [0.122]**	-0.420 (0.125)*** [0.114]***
Fixed Effects			
Year	X		
EEZ × Year		X	X
EEZ × Month	X	X	
EEZ × Month × Day			X
# Obs.	111,977	111,977	111,977

Notes: This table reports estimates of fishing ban impacts on log boat detections using three fixed-effects specifications. Each observation is an EEZ × day, with Chinese EEZ's four regulatory zones treated as separate EEZs. During 2012-2017, these zones implemented 24 fishing bans of varying duration (see Table 2). Column (1) includes EEZ-specific month fixed effects, Column (2) adds EEZ-specific year fixed effects, and Column (3) includes EEZ-specific day-of-the-year and year fixed effects. Two-way cluster-robust standard errors in parentheses allow for correlation within EEZ across dates and within date across EEZs (147 EEZ and 2,644 date clusters). Conley (1999) robust standard errors in brackets account for spatial correlation up to 1,000 km and serial correlation up to 35 nights. * $p < 0.10$; ** $p < 0.05$; *** $p < 0.01$.

only 10% significance using two-way cluster-robust standard errors. The estimated effects are generally smaller in magnitude than those reported in Tables A.1 and A.2 for ban initiation. This pattern is consistent with two complementary explanations: first, there are more frequent ban violations during the ban period compared to its onset; second, some fishing activities that would otherwise occur during the fishing bans are redistributed to the non-ban period. This temporal displacement of fishing effort helps explain why the difference-in-differences estimates, which capture average effects over longer periods, are smaller than the RD estimates that measure immediate responses to ban transitions.

5 Compliance during Fishing Bans

Analysis using AIS data (Figure A.4) shows stronger compliance with fishing bans compared to light-based detection methods. While vessels could potentially disable their AIS devices during illegal activities, examination of the Welch et al. (2022) AIS-disabling dataset suggests this is unlikely to bias my results. Chinese-flagged vessels predominantly disable AIS in international waters—particularly near Japanese and Peruvian EEZs—rather than within China's EEZ (Appendix Figure A.8). Moreover, non-

Chinese vessels rarely disable AIS near China's EEZ. The observed differences between AIS-based data and boat detections are thus more likely attributable to vessel size characteristics, as AIS-equipped vessels tend to be larger, rather than strategic AIS-disabling behavior.

While vessels could theoretically evade detection by operating without lights, several factors mitigate this concern. First, VIIRS can detect minimal light emissions, though subject to weather conditions. Second, since China's EEZ enforcement requires physical vessel inspection rather than mere detection, and given that maritime navigation cannot be prohibited, light concealment may offer limited benefits. Third, the persistent fishing activity by larger, AIS-equipped vessels suggests relatively low inspection risk. Nevertheless, the inability to quantify light-based evasion remains a limitation of my analysis.

The RD plots show increasing boat detections as fishing bans progress, which cannot be fully explained by improved weather conditions. This pattern suggests potential deterioration in ban effectiveness over time, which could stem from multiple factors.

First, enforcement intensity may decline during the ban period. While the Ministry of Agriculture sets national fishing regulations, enforcement is delegated to provincial agencies, potentially leading to varying enforcement patterns across regions and over time. Second, economic incentives for illegal fishing likely strengthen during the ban. Figure A.9 shows that frozen fish import prices peak in August, suggesting increased demand for seafood during the ban period.

To examine how fishing incentives affect compliance, I analyze the relationship between oceanographic conditions and vessel detection. [Axbard \(2016\)](#) shows that sea surface temperature and chlorophyll-a concentration affect fishing opportunities and income in Indonesia. However, the relationship between oceanographic conditions and fishing activity likely varies by region. To adapt this approach to the vast Chinese EEZ, I use LASSO regression to predict fishing opportunities based on sea surface temperature and chlorophyll-a concentration data from non-ban periods. Using out-of-sample LASSO predictions, I classify $1^\circ \times 1^\circ$ grid cells into areas with above- or below-median favorable fishing conditions.

Appendix Figure A.10 shows that, during the fishing ban, areas with favorable oceanographic conditions (above-median predicted boat detections) exhibit larger increases in actual detections during bans compared to less favorable areas.

Appendix Table A.4 compares boat detections between areas with above- and below-median fishing favorability during fishing bans. Since oceanographic conditions

vary over time, I include cell fixed effects to account for time-invariant location characteristics. Both types of areas see increased boat detections in the second half of the ban period. Areas with above-median fishing favorability show approximately 100% higher boat detections in the second half of the ban compared to their first-half levels, while areas with below-median favorability experience only a 34% increase. The difference in these increases is statistically significant at the 5% level. This pattern persists when using normalized duration as a more continuous measure of time, with the interaction term between normalized duration and favorable conditions significant at the 1% level. These patterns suggest that areas with more favorable fishing conditions systematically experience higher levels of fishing activity as bans progress.

I split the $1^\circ \times 1^\circ$ grid cells into two subsamples based on their above- or below-median out-of-sample predicted boat detections during fishing bans. I then re-estimate the baseline RDiT specification separately for these subsamples. Table A.5 shows that areas with higher predicted fishing favorability experience smaller discontinuities in boat detections at ban transitions. This pattern suggests that prime fishing grounds were more congested outside of fishing bans, consistent with economic incentives influencing ban compliance.

6 Spillovers and Displacement

My findings indicate that fishing bans reduce vessel detections within Chinese waters. However, these regulations may generate spillover effects beyond China's EEZ. Chinese vessels might fish illegally and opportunistically in neighboring EEZs outside of fishing bans. If fishing bans in Chinese EEZ lower trip profitability, or if port-based enforcement limits vessel mobility, Chinese fishing bans might decrease activity in neighboring EEZs. Alternatively, if Chinese vessels redirect their efforts to avoid domestic restrictions, neighboring waters could see increased activity during ban periods.

The environmental policy literature has documented substantial spatial spillovers and inter-jurisdictional externalities (see, e.g., [Burgess et al., 2012](#); [Kahn et al., 2015](#); [Lipscomb and Mobarak, 2016](#)). Given imperfect EEZ border enforcement, fishery regulations like China's seasonal bans may generate significant spillover or displacement effects.

To investigate whether fishing bans in the Chinese EEZ affect vessel activity in neighboring EEZs, I apply the start and end dates of regulatory zones in Chinese waters to boat detection data in neighboring EEZs. In the absence of inter-jurisdictional

spillovers, fishing bans in the Chinese EEZ should have no impact on boat detections in neighboring EEZs.

Appendix Figure A.11 presents RD plots analogous to the Chinese EEZ analysis in Figure A.3, but focuses on boat detections in adjacent EEZs. For Zone 1, neighboring EEZs include North Korean and partial South Korean waters; for Zone 2, neighboring areas comprise parts of South Korean, Japanese, and Taiwanese EEZs; Zone 3 borders portions of Japanese and Taiwanese EEZs; and Zone 4 adjoins parts of Taiwanese and Vietnamese EEZs. Following VBD data conventions, analysis of waters neighboring the Chinese EEZ is restricted to areas west of 126.5 degrees East.

When fishing bans begin in Zones 1 through 3, boat detections in their respective neighboring EEZs show modest but significant decreases. The lifting of these bans produces less pronounced increases in boat detections in bordering EEZs, with the exception of Zone 4's neighboring waters.

Appendix Table A.6 reports nonparametric RD estimates following the structure of Table A.2. While statistically significant decreases in boat detections occur in only three zones' neighboring waters when bans begin, point estimates are negative across all four zones at ban initiation and positive when bans are lifted. These results provide evidence that the Chinese fishing ban generates substantial spillover effects on vessel activity in neighboring EEZs.

The spillover to neighboring EEZs suggests that EEZ boundaries are not strictly enforced for fisheries regulation. This lack of strict enforcement aligns with the absence of spatial discontinuity in boat detection density around Chinese EEZ outer borders, as reported in Figure A.12. Outside the China-Vietnam border segment, Chinese waters show higher fishing intensity than neighboring EEZs during non-ban periods, with density increasing toward the Chinese shore. However, during fishing bans, boat density outside of Chinese EEZ becomes higher. Still, there is no spatial discontinuity at the EEZ borders.

Inter-jurisdictional spillover may also occur within Chinese EEZs. Prior to 2017, Zones 3 and 4 historically ended their bans earlier than Zones 1 and 2, and also started their bans earlier. Appendix Figure A.13 explores this inter-jurisdictional spillover within China. The RD plots on the left apply the earlier start dates in Zones 3 and 4 to boat detections in Zones 1 and 2 between 2012 and 2016, while the RD plots on the right apply the earlier end dates in Zones 3 and 4 to boat detections in Zones 1 and 2 between 2012 and 2017.

I find evidence that the start of fishing bans in Zones 3 and 4 reduces boat detec-

tions in Zones 1 and 2, though the RD estimates are not statistically significant at conventional levels. However, the end of fishing bans in Zones 3 and 4 is associated with increased boat detections in Zones 1 and 2. The nonparametric estimates for Zones 1 and 2 are statistically significant at the 1% and 10% levels, respectively. The point estimate for Zone 2, which is adjacent to Zone 3, is considerably larger than that for Zone 1.⁴

Nevertheless, the potential spillovers across regulatory zones and the challenges they pose to enforcing fishing bans were serious enough for Beijing to align the starting dates of fishing bans across all four zones in 2017.

Both boat detection data and AIS-based vessel counts demonstrate significant reductions in fishing activity during China's ban periods. While individual vessels might increase their fishing intensity, Figure A.4 shows that total fishing effort in China's EEZ remains substantially lower during bans. The impact extends beyond Chinese waters, as Figure A.14 reveals substantial drops in fishing hours by AIS-equipped Chinese vessels outside China's EEZ. This pattern holds globally, with Chinese-flagged vessels showing marked reductions in fishing hours at the start of ban periods (Figure A.15).

The evidence indicates substantial compliance with China's seasonal fishing bans, as a large proportion of Chinese vessels cease operations during ban periods. This reduction in fishing activity is most pronounced within China's EEZ, with smaller but notable decreases observed in neighboring EEZs.

While there is no evidence of short-term displacement, particularly increased fishing just before bans begin, fishing activity appears to be redistributed across non-ban months. This temporal displacement is most evident in September, the first month after all bans end, when Chinese fleet activity reaches its annual peak and exceeds the combined fishing effort of all other nations (Appendix Figure A.16). The pattern of temporal displacement spread across non-ban months, rather than concentrated around ban transitions, aligns with the observation that difference-in-differences estimates show smaller effects compared to RD estimates.

⁴It is important to note one confounding factor that cautions against a causal interpretation of these findings. Starting on August 1st, certain fishing methods were exempted in Zones 1 and 2, coinciding with the end of fishing bans in Zones 3 and 4 before 2017.

7 Foreign Fleets in Chinese Waters

While the previous section documented spillover effects of Chinese fishing bans on neighboring waters, the analysis also revealed that EEZ boundaries are not strictly enforced, with no clear spatial discontinuities in fishing activity at these borders. This suggests that not all vessels operating within China's EEZ are Chinese-flagged. Indeed, the AIS data allows us to directly examine this phenomenon, revealing that foreign vessels may opportunistically enter Chinese waters when domestic fishing activity is restricted.

Although Chinese vessels dominate fishing activity in the Chinese EEZ, the presence of foreign vessels nearly doubles from 0.9% during non-ban periods to 1.6% during ban periods. The change in fishing effort is even more pronounced: foreign vessels account for 0.7% of fishing hours in Chinese EEZ during non-ban periods but approximately 2% during ban periods. Vietnamese vessels provide a particularly striking example of this pattern. While they account for only 0.02% of fishing hours in Chinese EEZ during non-ban periods, their share increases to 0.33% during ban periods. Notably, this increase is not merely an artifact of reduced Chinese fishing activity in the denominator - the absolute number of fishing hours by Vietnamese vessels during the three-month ban period exceeds their total fishing hours during the approximately nine months outside the ban period.

The Gulf of Tonkin (Beibu Bay) represents a particularly active area for potential EEZ incursions. This region, divided between Vietnamese and Chinese EEZ, experiences intense fishing activity (as shown in Figure 1). High population density along both coasts, including proximity to major Vietnamese cities like Hanoi and Hai Phong, contributes to fishing pressure in these waters. The average distance between Vietnamese and Chinese shores in this area is less than 250 km, facilitating cross-border movement. Enforcement challenges are compounded by the Vietnamese fleet's characteristics: their vessels tend to be smaller than Chinese ones, even among AIS-equipped ships, suggesting a larger proportion of small vessels without AIS tracking capability. This combination of factors makes effective EEZ border patrol particularly challenging.

To examine whether EEZ boundaries effectively separate fishing activities, I analyze spatial patterns of boat density around these borders. Using $5 \text{ km} \times 5 \text{ km}$ grid cells, I calculate boat detections per square kilometer per week, separately for ban and non-ban periods (as in Figure A.12 for EEZ borders outside the China-Vietnam segment). A.17 shows that along the China-Vietnam border, Vietnamese waters exhibit higher

fishing density, with no clear discontinuity at the border during either ban or non-ban periods.

To formally test for spatial discontinuities, I employ the [Cattaneo et al. \(2020\)](#) local polynomial density estimator, which improves upon the [McCrary \(2008\)](#) approach by eliminating the need for pre-binning. Appendix Figure A.18 presents these results, showing no significant discontinuity in boat density at the China-Vietnam border during ban periods (p -value = 0.815). Similar tests for other segments of China's EEZ boundary yield similarly no significant discontinuity in boat density.

These patterns suggest that EEZ boundaries are not effectively enforced, particularly during fishing bans. The increased presence of foreign vessels during Chinese bans presents challenges for policy effectiveness. While the bans successfully reduce overall fishing activity, the entry of foreign vessels may partially offset the intended conservation benefits. This finding highlights the importance of international cooperation in fisheries management, particularly given the mobile nature of both fish stocks and fishing fleets.

8 Concluding Remarks

This paper examines the effectiveness of China's seasonal fishing bans in curbing fishing activities within its Exclusive Economic Zone (EEZ). The findings indicate that the bans, though not perfectly enforced, lead to significant reductions in both boat detections and fishing hours during the ban periods. This impact highlights the potential of command-and-control policies for resource management in contexts where market-based mechanisms may be challenging to implement.

Several complementary factors likely enhance the effectiveness of these bans, including coordinated offshore patrols, inspections, and the availability of aquaculture alternatives that mitigate consumer demand during the ban period. However, some evidence suggests that enforcement effectiveness declines over time, with fishing activities gradually resuming toward the later stages of the bans.

The study also underscores the importance of considering inter-jurisdictional spillovers. Chinese vessels operating in neighboring EEZs during ban periods and foreign vessels increasing their activities in the Chinese EEZ suggest that cooperation with adjacent nations could enhance policy efficacy.

Overall, this analysis contributes to understanding the conditions under which seasonal fishing bans can achieve sustainable fishery objectives. Further research could

examine heterogeneity in ban compliance across different vessel types and explore additional regulatory tools to complement seasonal bans.

References

- Assunção, Juliano, Clarissa Gandour, and Romero Rocha (2023) "DETER-ing Deforestation in the Amazon: Environmental Monitoring and Law Enforcement," *American Economic Journal: Applied Economics*, 15 (2), 125–56.
- Axbard, Sebastian (2016) "Income Opportunities and Sea Piracy in Indonesia: Evidence from Satellite Data," *American Economic Journal: Applied Economics*, 8 (2), 154–194.
- Barreca, Alan I., Melanie Guldi, Jason M. Lindo, and Glen R. Waddell (2011) "Saving Babies? Revisiting the Effect of Very Low Birth Weight Classification," *Quarterly Journal of Economics*, 126, 2117–2123.
- Besley, Timothy, Thiemo Fetzer, and Hannes Mueller (2015) "The Welfare Cost of Lawlessness: Evidence from Somali Piracy," *Journal of the European Economic Association*, 13 (2), 203–239.
- Bos, Björn (2021) "Fishing under the Radar: Estimating Compliance with Fishing Bans," September, 10.2139/ssrn.3871993, Available at SSRN: <https://ssrn.com/abstract=3871993>.
- Brown, Gardner M (2000) "Renewable Natural Resource Management and Use Without Markets," *Journal of Economic Literature*, 38 (4), 875–914.
- Burgess, Robin, Matthew Hansen, Benjamin A. Olken, Peter Potapov, and Stefanie Sieber (2012) "The Political Economy of Deforestation in the Tropics," *Quarterly Journal of Economics*, 127 (4), 1707–1754, 10.1093/qje/qjs034.
- Calonico, Sebastian, Matias D Cattaneo, and Rocio Titiunik (2014) "Robust Nonparametric Confidence Intervals for Regression-Discontinuity Designs," *Econometrica*, 82 (6), 2295–2326.
- Carruthers, Bruce G and Naomi R Lamoreaux (2016) "Regulatory races: the effects of jurisdictional competition on regulatory standards," *Journal of Economic Literature*, 54 (1), 52–97.
- Cattaneo, Matias D, Michael Jansson, and Xinwei Ma (2020) "Simple Local Polynomial Density Estimators," *Journal of the American Statistical Association*, 115 (531), 1449–1455.
- Chan, H Ron and Christy Zhou (2023) "Charged Up? Distributional Impacts of Green Energy on Local Labor Markets," *SSRN Working Paper*, https://papers.ssrn.com/sol3/papers.cfm?abstract_id=4534479.
- Chan, H Ron and Yichen Christy Zhou (2021) "Regulatory Spillover and Climate Co-benefits: Evidence From New Source Review Lawsuits," *Journal of Environmental Economics and Management*, 110, 102545.

- China Fishery Statistical Year Book (2016) *China Fishery Statistical Year Book*: China Agriculture Press.
- Conley, Timothy G (1999) "GMM Estimation with Cross Sectional Dependence," *Journal of Econometrics*, 92 (1), 1–45.
- Cropper, Maureen L and Wallace E Oates (1992) "Environmental Economics: A Survey," *Journal of Economic Literature*, 30 (2), 675–740.
- Donaldson, Dave and Adam Storeygard (2016) "The View from Above: Applications of Satellite Data in Economics," *Journal of Economic Perspectives*, 30 (4), 171–98.
- Elvidge, Christopher D, Kimberly E Baugh, Mikhail Zhizhin, and Feng-Chi Hsu (2013) "Why VIIRS Data Are Superior to Dmsp for Mapping Nighttime Lights," *Proceedings of the Asia-Pacific Advanced Network*, 35, 62–69.
- Elvidge, Christopher D, Kimberly Baugh, Mikhail Zhizhin, Feng Chi Hsu, and Tilotama Ghosh (2017) "VIIRS Night-time Lights," *International Journal of Remote Sensing*, 38 (21), 5860–5879, 10.1080/01431161.2017.1342050.
- Elvidge, Christopher D, Mikhail Zhizhin, Kimberly Baugh, and Feng-Chi Hsu (2015a) "Automatic Boat Identification System for VIIRS Low Light Imaging Data," *Remote Sensing*, 7 (3), 3020–3036.
- Elvidge, Christopher D, Mikhail Zhizhin, Kimberly Baugh, Feng-Chi Hsu, and Tilotama Ghosh (2015b) "Methods for Global Survey of Natural Gas Flaring from Visible Infrared Imaging Radiometer Suite Data," *Energies*, 9 (1), 14.
- Flückiger, Matthias and Markus Ludwig (2015) "Economic Shocks in the Fisheries Sector and Maritime Piracy," *Journal of Development Economics*, 114, 107–125.
- Hausman, Catherine and David S Rapson (2018) "Regression Discontinuity in Time: Considerations for Empirical Applications," *Annual Review of Resource Economics*, 10, 533–552.
- He, Guojun, Shaoda Wang, and Bing Zhang (2020) "Watering Down Environmental Regulation in China," *Quarterly Journal of Economics*, 135 (4), 2135–2185.
- Henderson, J. Vernon, Adam Storeygard, and David N. Weil (2012) "Measuring Economic Growth from Outer Space," *American Economic Review*, 102 (2), 994–1028, 10.1257/aer.102.2.994.
- Hodler, Roland and Paul A. Raschky (2014) "Regional Favoritism," *Quarterly Journal of Economics*, 129 (2), 995–1033, 10.1093/qje/qju004.
- Hu, Chuanmin, Lian Feng, Zhongping Lee, Bryan A Franz, Sean W Bailey, P Jeremy Werdell, and Christopher W Proctor (2019) "Improving satellite global chlorophyll a data products through algorithm refinement and data recovery," *Journal of Geophysical Research: Oceans*, 124 (3), 1524–1543.

- Kahn, Matthew E, Pei Li, and Daxuan Zhao (2015) "Water Pollution Progress at Borders: the Role of Changes in China's Political Promotion Incentives," *American Economic Journal: Economic Policy*, 7 (4), 223–42.
- Kroodsma, David A, Juan Mayorga, Timothy Hochberg et al. (2018) "Tracking the global footprint of fisheries," *Science*, 359 (6378), 904–908.
- Lipscomb, Molly and Ahmed Mushfiq Mobarak (2016) "Decentralization and Pollution Spillovers: Evidence from the Re-Drawing of County Borders in Brazil," *Review of Economic Studies*, 84 (1), 464–502.
- McCrory, Justin (2008) "Manipulation of the Running Variable in the Regression Discontinuity Design: A Density Test," *Journal of Econometrics*, 142 (2), 698–714.
- Michalopoulos, Stelios and Elias Papaioannou (2013) "National Institutions and Sub-national Development in Africa," *Quarterly Journal of Economics*, 129 (1), 151–213.
- Ministry of Agriculture (2017) "Most Restrictive Fishing Conservation Policy Protects Marine Fishery Resources," *Press Office of the Chinese Ministry of Agriculture*, http://jiuban.moa.gov.cn/zwl1m/zwdt/201708/t20170803_5768337.htm.
- Ministry of Agriculture and Rural Affairs (2019) 2019 [China Fishery Statistical Yearbook 2019], Beijing: China Agriculture Press.
- Newey, Whitney K. and Kenneth D. West (1986) "A Simple, Positive Semi-definite, Heteroskedasticity and Autocorrelation Consistent Covariance Matrix," *Econometrica*, 55 (3), 703–08.
- Sigman, Hilary (2002) "International Spillovers and Water Quality in Rivers: Do Countries Free Ride?" *American Economic Review*, 92 (4), 1152–1159.
- U.N. Food and Agriculture Organization (2014) "The State of World Fisheries and Aquaculture," *FAO Fisheries and Aquaculture Department*.
- (2016) "The State of World Fisheries and Aquaculture," *FAO Fisheries and Aquaculture Department*.
- Walker, W Reed (2011) "Environmental regulation and labor reallocation: Evidence from the Clean Air Act," *American Economic Review*, 101 (3), 442–447.
- Watson, Reg and Daniel Pauly (2001) "Systematic Distortions in World Fisheries Catch Trends," *Nature*, 414 (6863), 534.
- Welch, Heather, Tyler Clavelle, Timothy D. White, Megan A. Cimino, Jennifer Van Osdell, Timothy Hochberg, David Kroodsma, and Elliott L. Hazen (2022) "Hot Spots of Unseen Fishing Vessels," *Science Advances*, 8 (44), eabq2109, 10.1126/sciadv.abq2109.
- Yan, Zhaojin, Rong He, Xiaoguang Ruan, and Hui Yang (2022) "Footprints of Fishing Vessels in Chinese Waters Based on Automatic Identification System Data," *Journal of Sea Research*, 187, 102255, 10.1016/j.seares.2022.102255.

Online Appendices

Table of Contents

1	Introduction	2
2	Background	4
2.1	Fishing Ban: Why?	4
2.2	Fishing Ban: When and Where?	5
2.3	Fishing Ban: How?	5
3	Data Description	6
3.1	VIIRS Boat Detection Data	6
3.2	Cloud Cover & Oceanographic Conditions	7
3.3	AIS-based Measures of Fishing Activities	8
4	Effectiveness of Fishing Bans	8
4.1	Parametric Estimation with RDiT Design	8
4.2	Graphic Representation and Non-parametric Estimation of RDiT	10
4.3	Validity and Robustness of the RDiT Design	12
4.4	Difference-in-Differences Estimation	13
5	Compliance during Fishing Bans	15
6	Spillovers and Displacement	17
7	Foreign Fleets in Chinese Waters	20
8	Concluding Remarks	21
References		23
A	Appendix A: Additional Figures and Tables	4
B	Appendix B: Data Description	28
B.1	VIIRS Boat Detection Data	28
B.2	Cloud Cover	31
B.3	NASA Ocean Color	31
B.4	AIS-based Measures of Fishing Efforts	32
B.5	AIS-disabling Events	33
B.6	Import Price of Frozen Fish	33

B.7	EEZ Boundaries	34
-----	----------------	----

List of Figures

1	Boats at Night	7
2	Boat Detected at Night around the Imposition and Lifting of Fishing Bans	11
A.1	Chinese EEZ, Fishery Regulatory Zones, and Neighboring EEZs	4
A.2	Randomization Inference	5
A.3	Discontinuity Changes in Boat Detection by Regulatory Zone around Starts and Ends of Fishing Bans	6
A.4	Fishing Effort based on AIS Signals around the Starts and Ends of Fishing Bans	7
A.5	Vessel Counts based on AIS Signals around the Starts and Ends of Fishing Bans: by Zone & by Vessel Flag	8
A.6	Continuity Tests and Plots with Oceanographic Variables	9
A.7	Placebo RDiT due to Shifting Start and End Dates of Fishing Ban	10
A.8	Location of AIS Disabling Events of Chinese-flagged Vessels	11
A.9	Average Import Price of Frozen Fish into China	12
A.10	Boat Detections during Fishing Ban by Oceanographic Conditions	13
A.11	RDiT of Boat Detections in Neighboring EEZs	14
A.12	Boat Density at China's EEZ Boundaries (Excluding China-Vietnam Border)	15
A.13	Spillover from Zones 3 & 4 to Zones 1 & 2	16
A.14	Fishing Hours of Chinese Fleets outside of Chinese EEZ around the Starts and Ends of Fishing Bans	17
A.15	Global Fishing Hours of Chinese Fleets around Transitions of Fishing Bans	18
A.16	Global Fishing Efforts by Month	19
A.17	Boat Density around the China-Vietnam EEZ Boundary	20
A.18	Spatial Continuity of Boat Density around the China-Vietnam EEZ Boundary	21

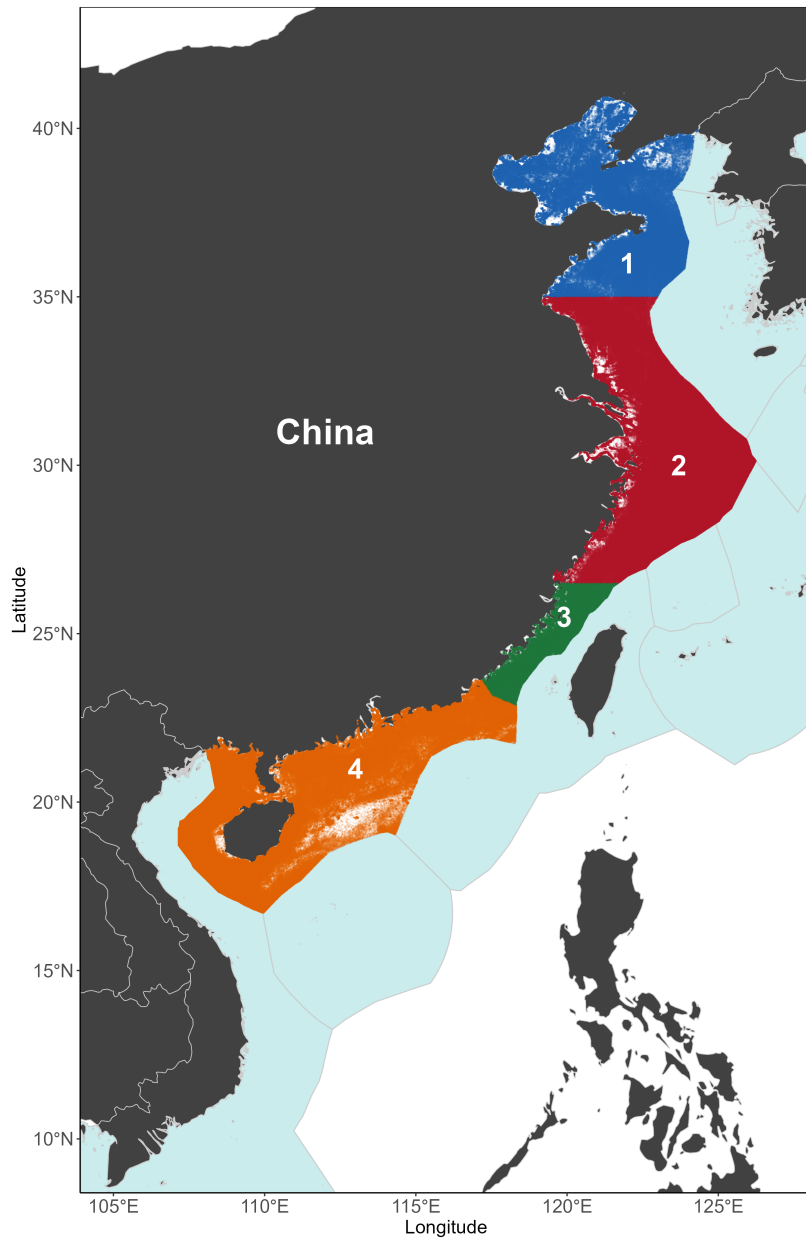
List of Tables

1	Number of Seafaring Fishing Vessels by Size	5
2	Effective Dates of Fishing Bans	6
3	Fishing Ban and the Number of Boats Detected: RDiT Estimates	9

4	Difference-in-Differences Estimates of Fishing Ban on Boat Detections	15
A.1	Fishing Ban and the Number of Boats Detected: RDiT Estimates by Zone	22
A.2	Fishing Ban and the Number of Boats Detected: Nonparametric RDiT Estimates	23
A.3	Fishing Ban and the Number of Boats Detected: Nonparametric Donut Hole RD Estimates	24
A.4	Boat Detections During Fishing Ban by Oceanographic-based Prediction	25
A.5	RDiT Estimates on Boats Detected by Fishing Favorability	26
A.6	Fishing Ban and the Number of Boats Detected in Neighboring EEZs: Nonparametric RD Estimates	27

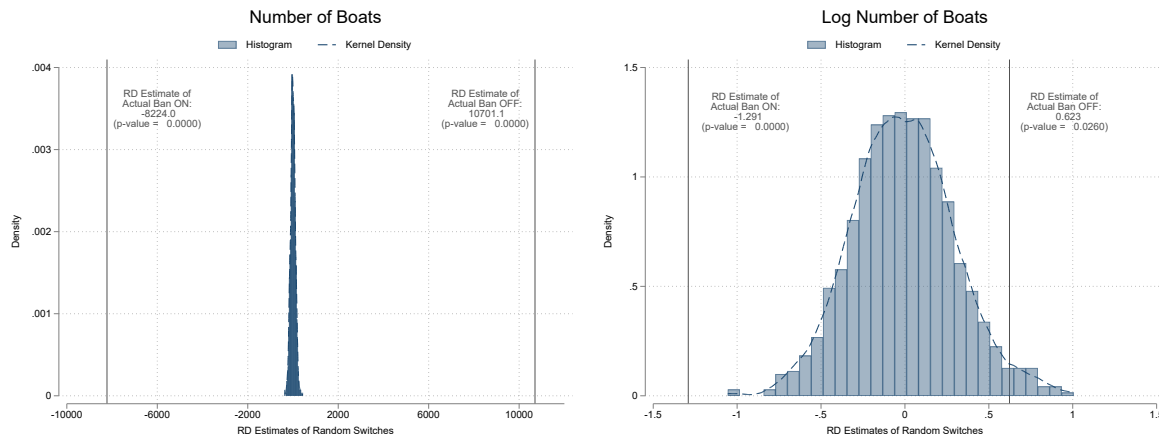
A Appendix A: Additional Figures and Tables

Figure A.1: Chinese EEZ, Fishery Regulatory Zones, and Neighboring EEZs



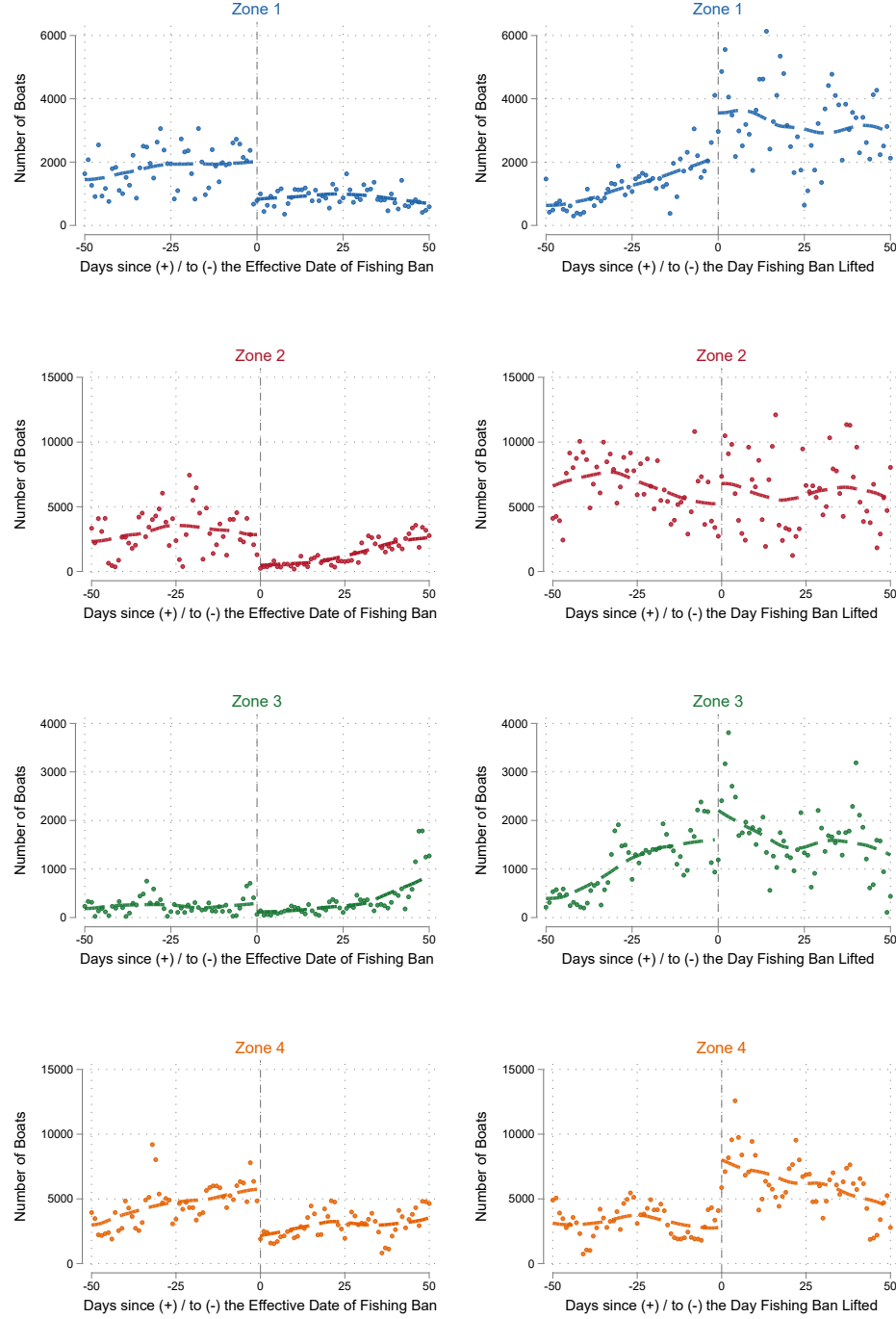
Notes: This map shows China's four fishery regulatory zones within its EEZ (Zones 1-4, colored), along with neighboring countries' EEZs and disputed areas (light blue). Zone 1 includes the Northern Yellow Sea north of N 35°. Zone 2 includes the southern Yellow Sea and the Northern East China Sea between N 35° and N 26°30'. Zone 3 includes the southern East China Sea between N 26°30' and the Min-Yue marine boundary. Zone 4 includes the Taiwan Strait and the South China Sea north of N 12°. EEZ boundaries are from Marine Regions' World EEZ Version 8.

Figure A.2: Randomization Inference



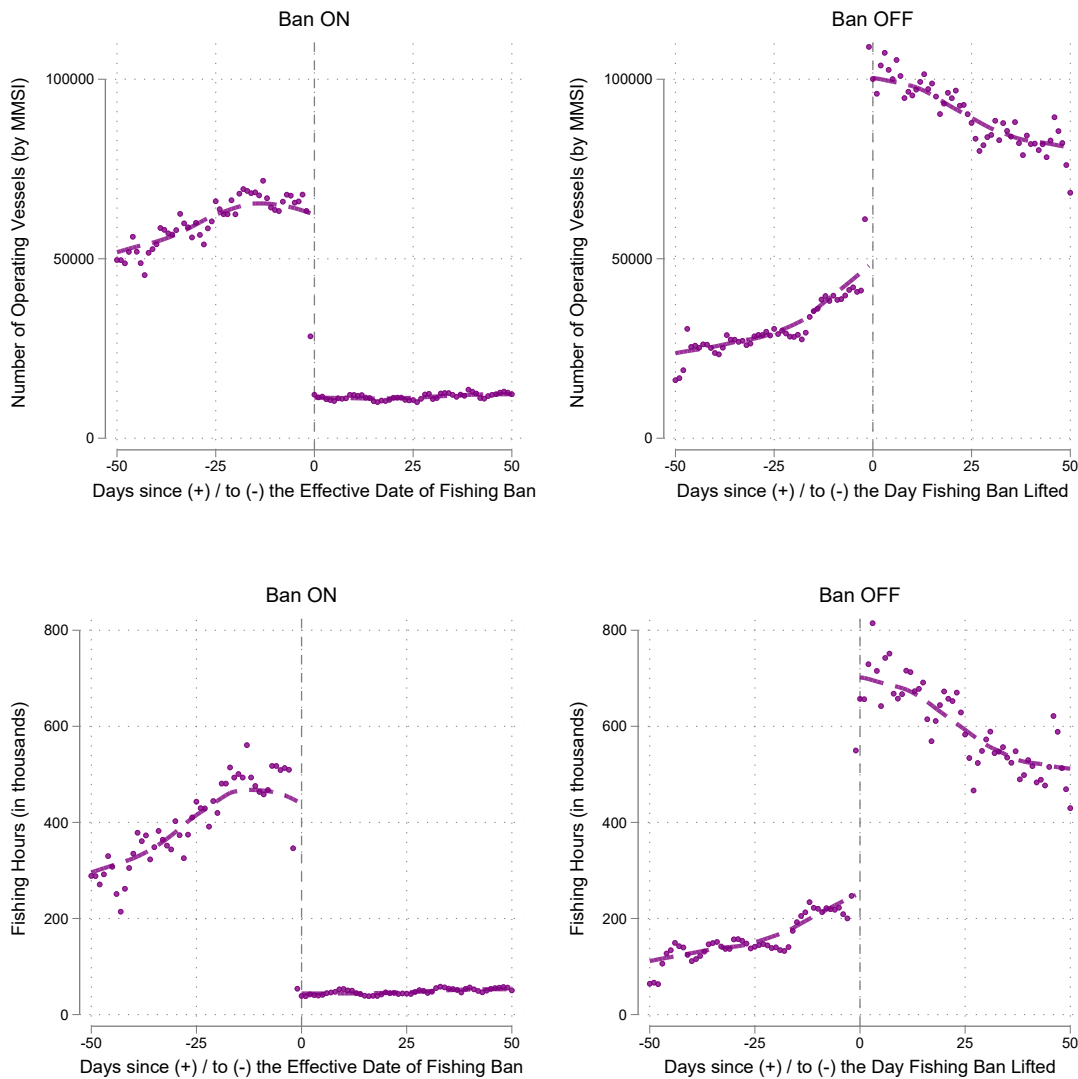
Notes: Notes: Distribution of placebo estimates from 1,000 simulations with randomized ban dates. Left: boat detection counts; right: log boat detections. Vertical lines show actual RD estimates with corresponding p-values from randomization inference. The simulation randomizes ban start and end dates across regulatory zones and years, creating a running variable similar to that used in the main analysis. This approach addresses potential concerns about time-series correlation that standard RD inference procedures may not fully account for.

Figure A.3: Discontinuity Changes in Boat Detection by Regulatory Zone around Starts and Ends of Fishing Bans



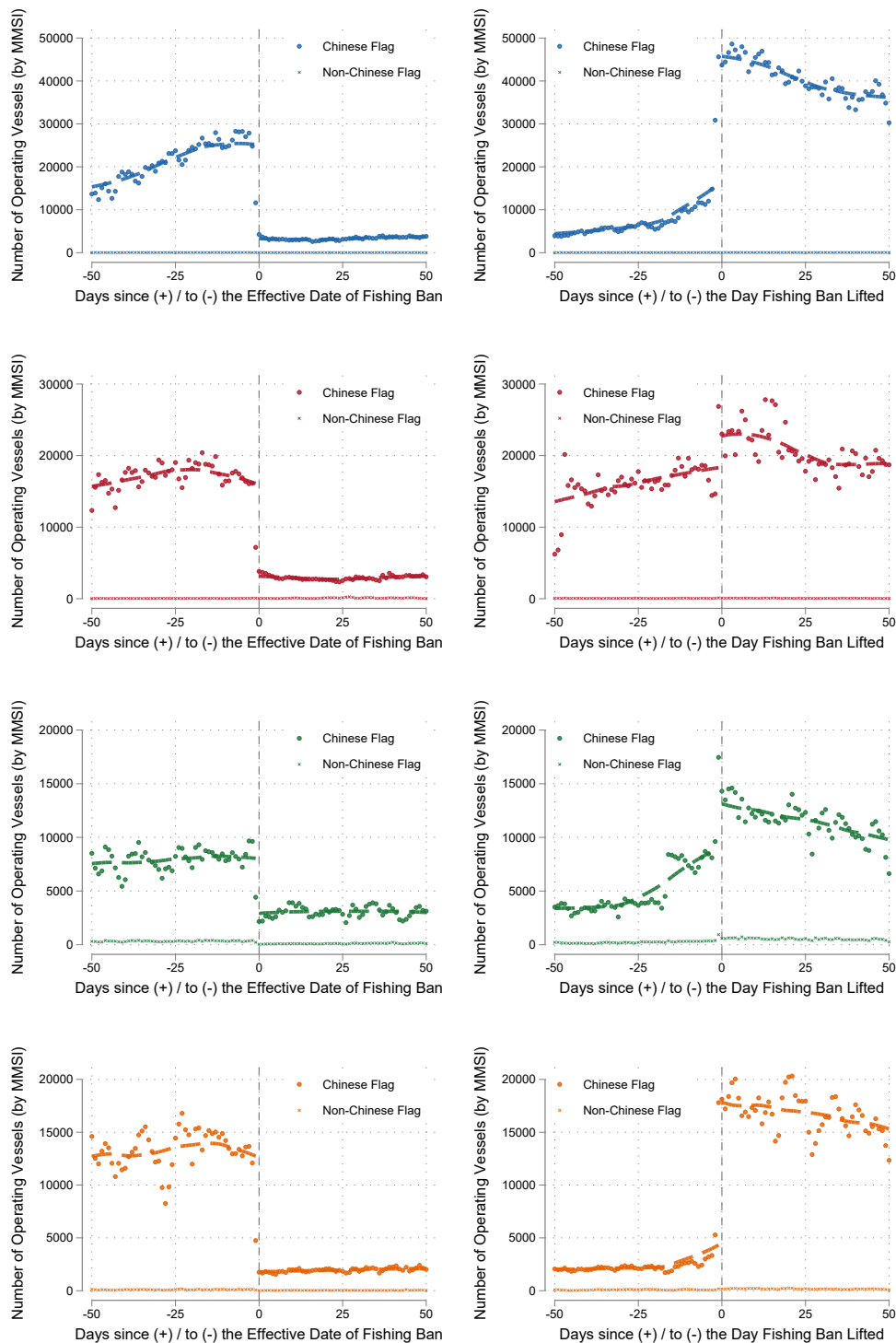
Notes: The RD graphs above are similar to Figure 2 but separately for each zone. The subplots on the left hand side concern the starting of fishing bans; the subplots on the right hand side concern the lifting of fishing bans. Rows 1 to 4 represents Zones 1 to 4 respectively. Each dot represents the number of boat detections across the respective regulatory zone τ nights since (+) or before (-) the fishing bans became effective (left subplots) or were lifted (right subplots). Night 0 is the first night after the fishing bans were lifted and the horizontal axis represents τ . The vertical axis represents the nightly number of boat detections aggregated over years from 2012 to 2017.

Figure A.4: Fishing Effort based on AIS Signals around the Starts and Ends of Fishing Bans



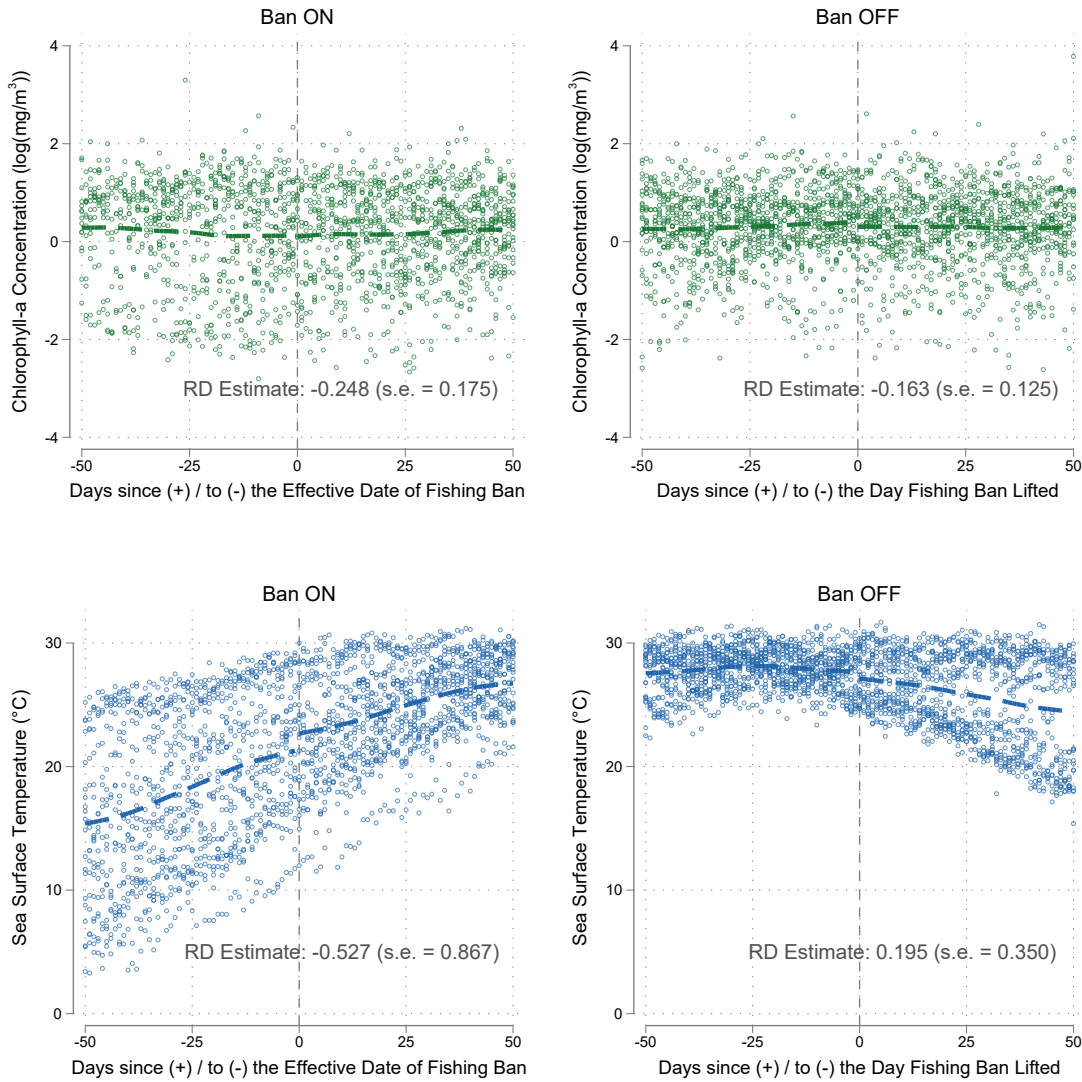
Notes: This figure shows RD plots examining two measures of fishing activity around China's fishing ban transitions. The top panels show the number of unique fishing vessels (by MMSI) detected in Chinese EEZ; the bottom panels show total fishing hours (in thousands). Left panels examine changes when bans begin ("Ban ON"); right panels show changes when bans end ("Ban OFF"). Each point represents daily aggregated activity across all regulatory zones, averaged across years 2012-2020. Day 0 marks the transition date, with the x-axis showing 50 days before and after transitions. Data are from Global Fishing Watch's AIS-based fishing effort dataset, aggregated from 0.1-degree grid cells matched to Chinese regulatory zones. Dashed lines show local polynomial fits on each side of the cutoff.

Figure A.5: Vessel Counts based on AIS Signals around the Starts and Ends of Fishing Bans: by Zone & by Vessel Flag



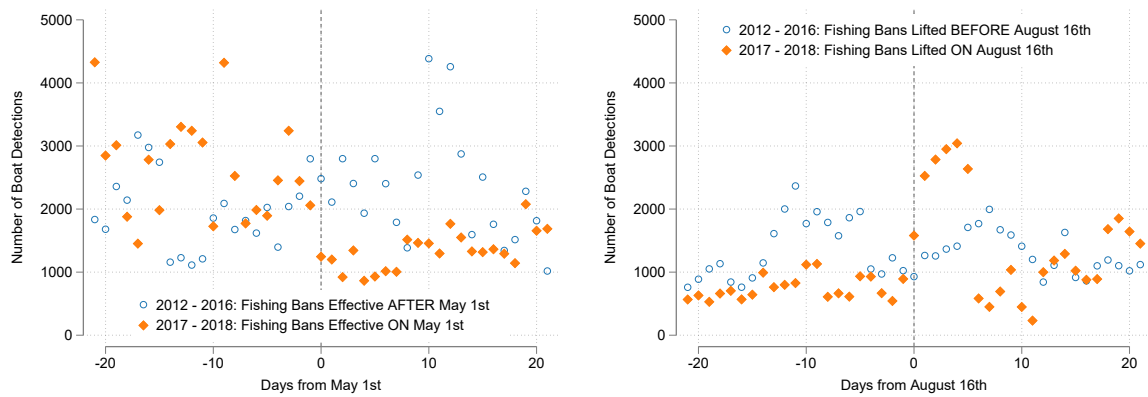
Notes: This figure shows RD plots examining the number of operating fishing vessels (identified by MMSI) separately for Chinese and non-Chinese flagged vessels in each regulatory zone. Each row represents a different zone (Zones 1-4 from top to bottom). Left panels show changes when bans begin; right panels show changes when bans end. Blue/red/green/orange dots represent Chinese-flagged vessels; gray dots represent non-Chinese flagged vessels. Each point represents the daily count of unique vessels operating in the zone, aggregated across years 2012-2020. Day 0 marks the transition date, with the x-axis showing 50 days before and after transitions. Dashed lines show local polynomial fits.

Figure A.6: Continuity Tests and Plots with Oceanographic Variables



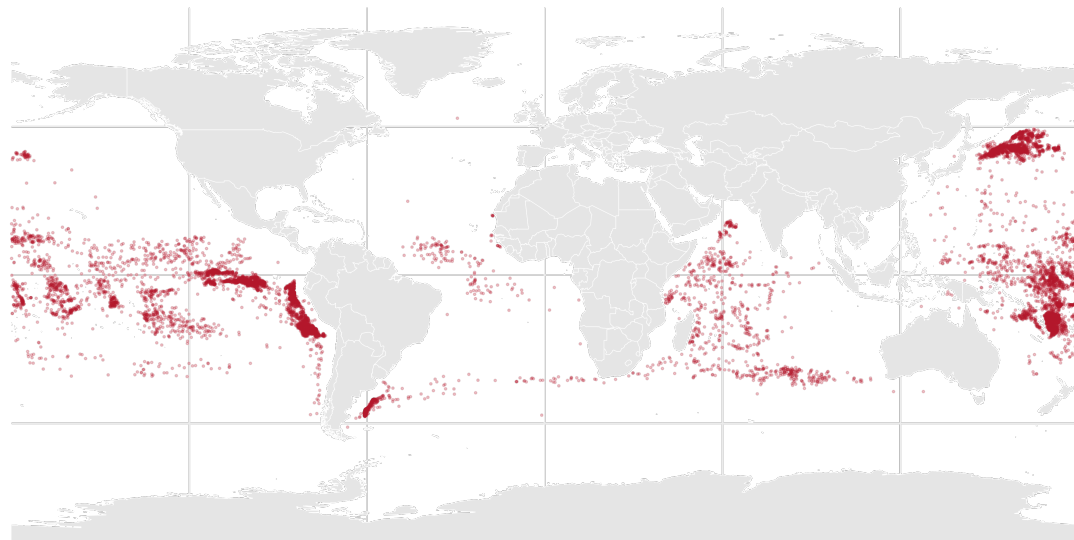
Notes: This figure presents RD plots testing for discontinuities in oceanographic conditions around the start and end dates of China's fishing bans from 2012-2017. The top panels show log chlorophyll-a concentration (mg/m^3), and bottom panels show sea surface temperature ($^\circ\text{C}$), both derived from NASA Ocean Color VIIRS satellite data at daily frequency. Left panels examine discontinuities when bans begin ("Ban ON"); right panels when bans end ("Ban OFF"). Data points represent daily zone-level averages aggregated from the original $9 \text{ km} \times 9 \text{ km}$ resolution. The x-axis shows days relative to ban transitions, with day 0 marking the start/end of bans. Dashed lines show linear fits on each side of the cutoff. Non-parametric RD estimates and standard errors are reported for each discontinuity test.

Figure A.7: Placebo RDiT due to Shifting Start and End Dates of Fishing Ban



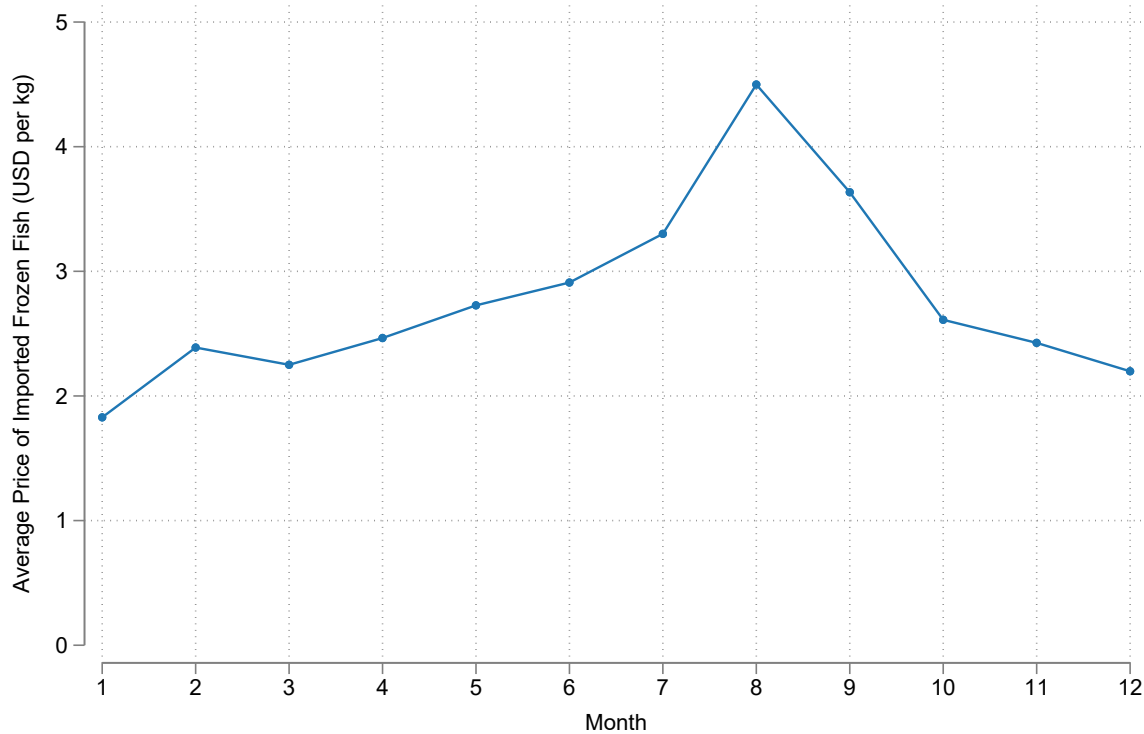
Notes: This figure presents placebo tests exploiting policy changes in China's seasonal fishing ban timing. The left panel examines the standardization of ban start dates to May 1st in 2017 (previously June 1st for Zones 1-2 and May 16th for Zones 3-4). The right panel examines the extension of ban end dates to August 16th in 2017 for Zones 3-4 (previously August 1st). Orange diamonds show daily boat detections in 2017-2018 when new dates applied; blue hollow circles show 2012-2016 when old dates applied. Day 0 marks May 1st in the left panel and August 16th in the right panel. The x-axis spans 20 days before and after these dates. Values represent average daily boat detections within each policy regime. Sample covers four regulatory zones where seasonal fishing bans are implemented. Running the same specifications as in Table A.1 with the placebo dates yields no statistically significant estimates for the Fishing Ban indicator.

Figure A.8: Location of AIS Disabling Events of Chinese-flagged Vessels



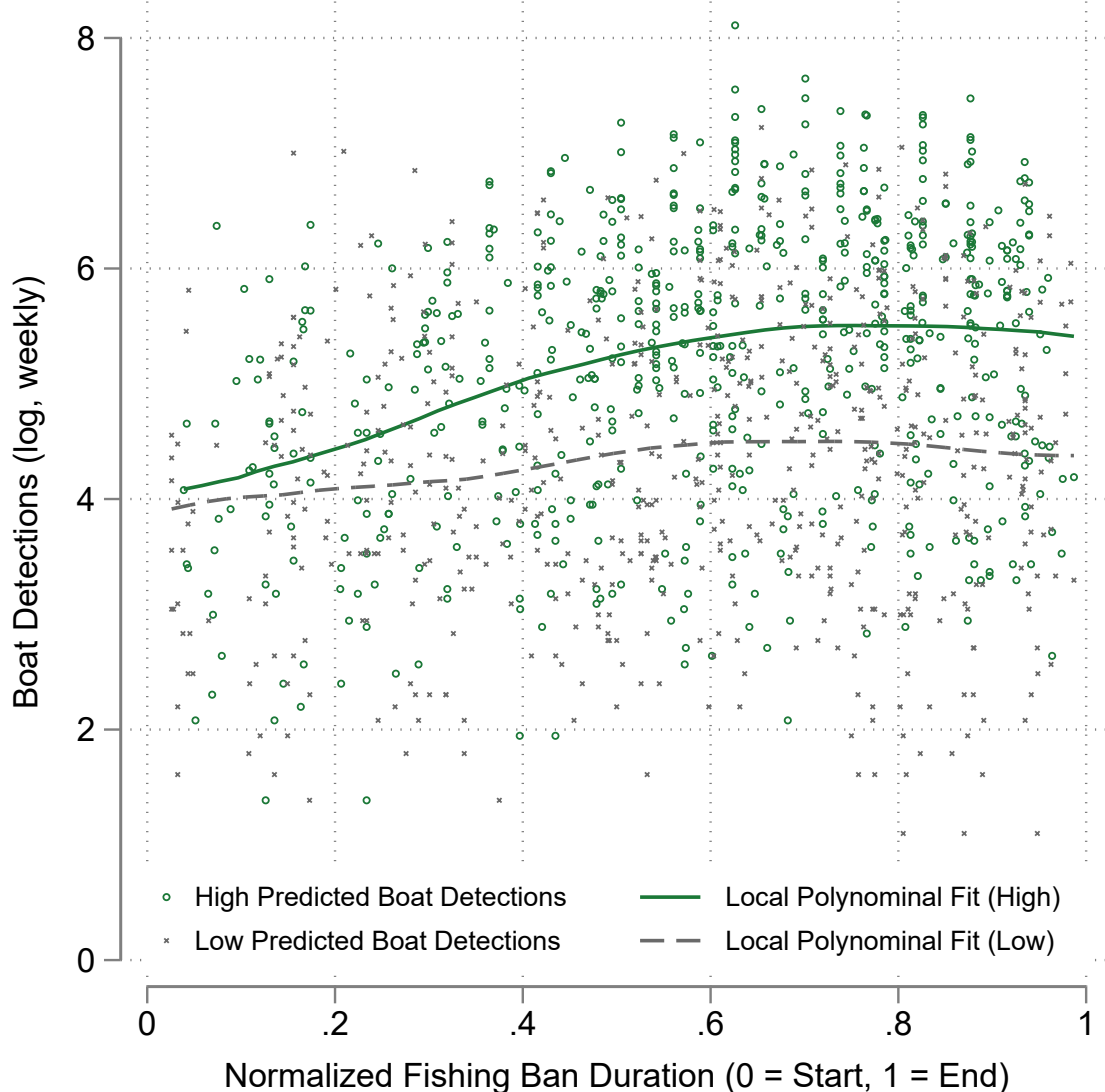
Notes: This figure maps the locations of Automatic Identification System (AIS) disabling events for Chinese-flagged vessels from 2017–2020, based on data from Global Fishing Watch analyzed by Welch et al. (2022). Red dots indicate locations where vessels are suspected to have intentionally disabled their AIS transmissions. The full dataset includes over 55,000 suspected disabling events occurring more than 50 nautical miles from shore, identified using a rule-based machine learning classification model applied to 3.7 billion AIS messages. AIS disabling events by Chinese vessels appear concentrated in international waters, particularly near the Japanese and Peruvian EEZs, with notably fewer events occurring within or near China's own EEZ. This pattern suggests that AIS disabling behavior by Chinese vessels may be driven more by fishing opportunities in distant waters than by attempts to evade domestic regulations.

Figure A.9: Average Import Price of Frozen Fish into China



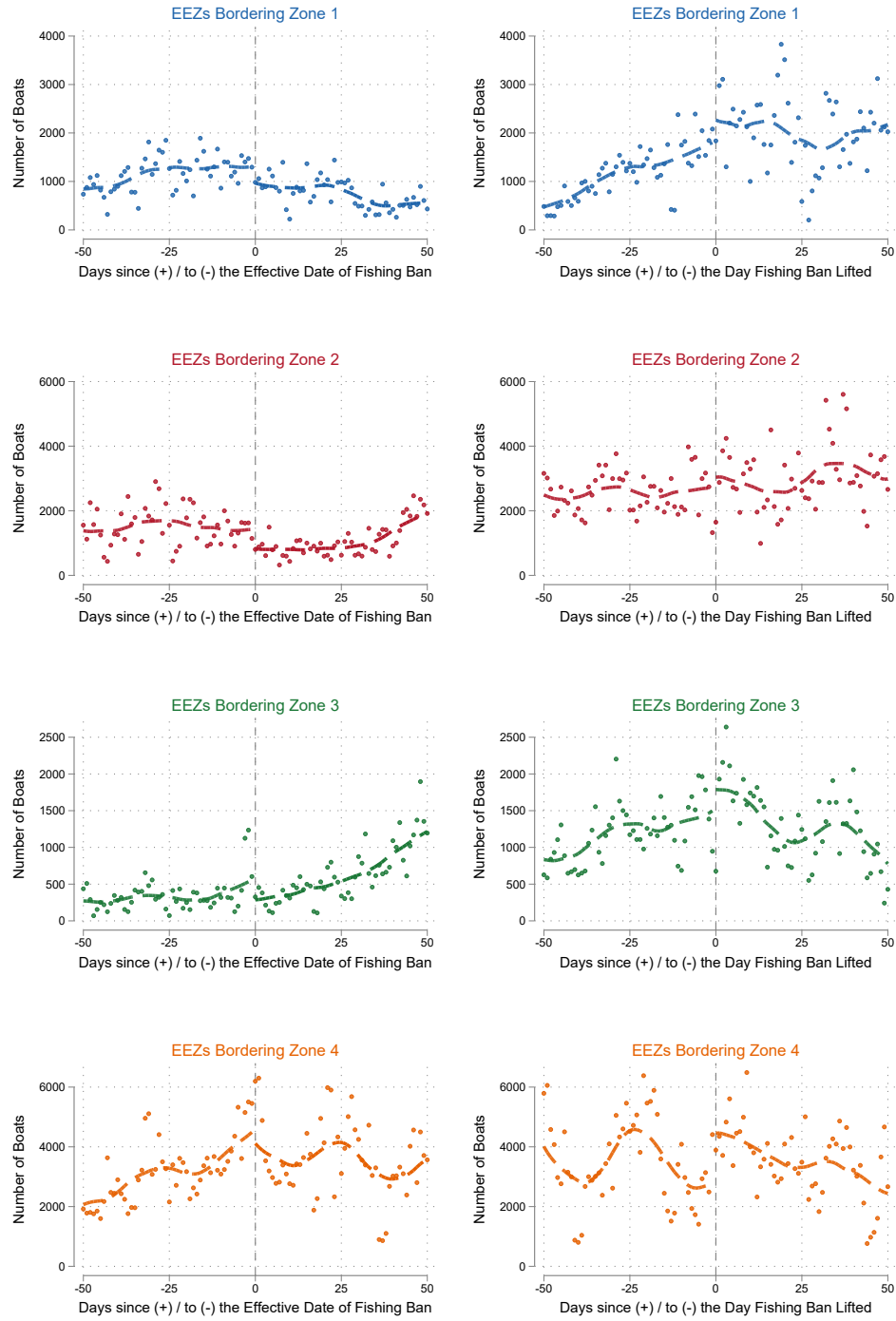
Notes: The figure shows the monthly average import price of frozen fish into China. The trade statistics are sourced from the United Nations Comtrade platform. China does not report import statistics to Comtrade at a monthly frequency. Instead, I accessed data via Comtrade's public API, using export values and volumes (weight) reported by the top 20 seafood exporters to China, based on annual trade data. The sample period spans from 2010 to 2017. Using data from these top 20 exporters, I calculated the average monthly import price of seafood in USD per kg. The top five seafood exporters to China during this period were Russia, the U.S., Canada, Norway, and New Zealand.

Figure A.10: Boat Detections during Fishing Ban by Oceanographic Conditions



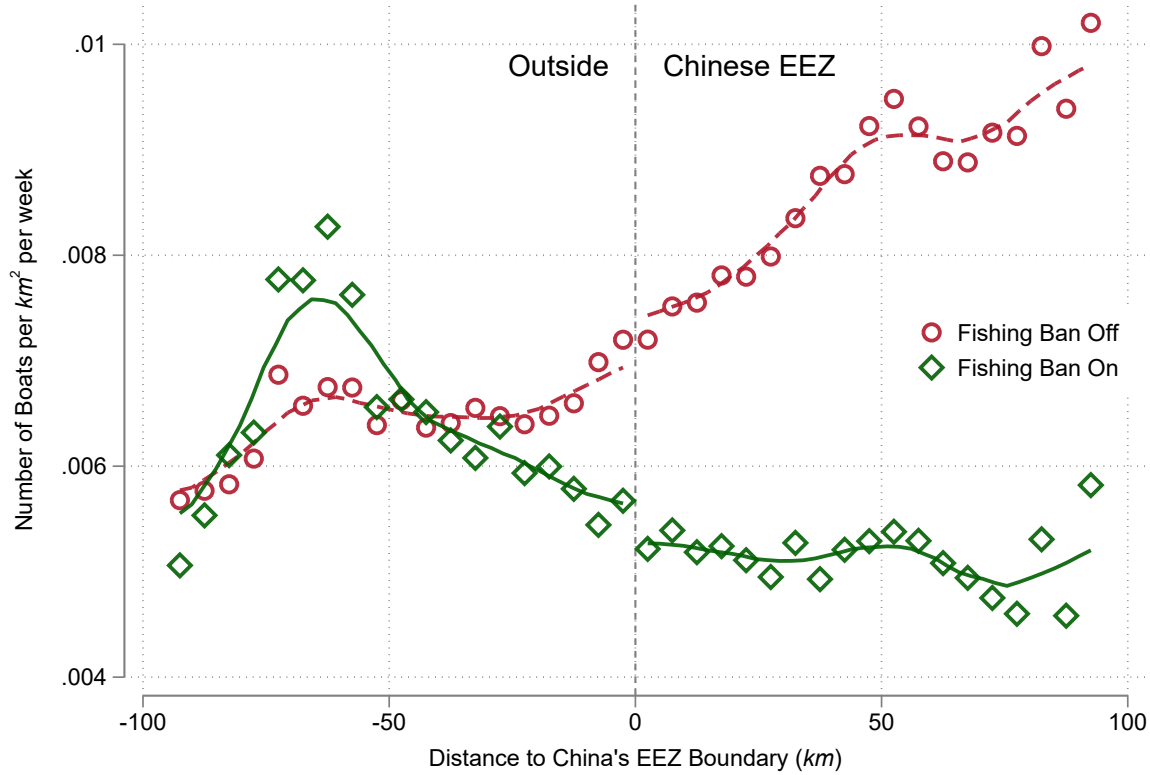
Notes: This figure plots boat detections during fishing bans against normalized ban duration (0 = start, 1 = end of ban), separately for areas with high and low predicted fishing opportunities based on oceanographic conditions. The y-axis shows log weekly boat detections in $1^\circ \times 1^\circ$ cells. Predictions are generated from a LASSO regression estimated on observations outside of fishing bans between 2012 and 2017. The LASSO model uses latitude-specific cubic polynomials of mean sea surface temperature, latitude-specific cubic polynomials of mean chlorophyll-a concentration, and their interaction polynomials up to degree three as predictors. The regularization parameter is selected using 10-fold cross-validation on the non-ban sample. High (low) predicted detections indicate above (below) median predicted values from this out-of-sample prediction during ban periods. Given varying ban durations across zones and years (77-138 days), time is normalized by ban length. Green circles and solid line represent areas with high predicted fishing opportunities; gray dots and dashed line show areas with low predicted opportunities. Lines show local polynomial fits. Areas with low predicted boat detections show modest increases in actual detections during ban periods, while those predicted to have high boat detections exhibit substantially larger increases, suggesting that favorable oceanographic conditions influence potential illegal fishing during bans, with effects intensifying as the ban progresses.

Figure A.11: RDiT of Boat Detections in Neighboring EEZs



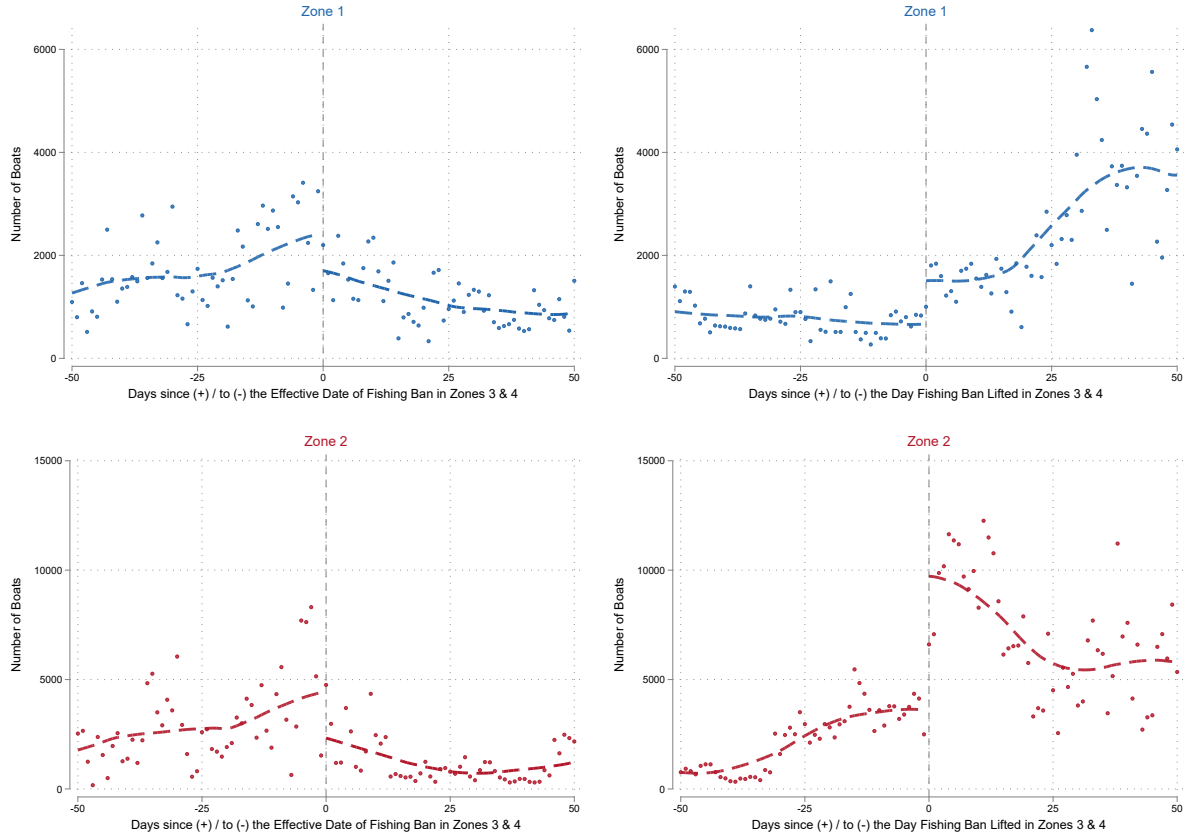
Notes: This figure shows RD plots examining boat detections in EEZs neighboring Chinese regulatory zones around China's fishing ban transitions. Each row represents a different Chinese regulatory zone and its neighboring EEZs: Zone 1 (North Korea, South Korea), Zone 2 (South Korea, Japan, Taiwan), Zone 3 (Japan, Taiwan), and Zone 4 (Taiwan, Vietnam). Left panels show changes when Chinese bans begin; right panels show changes when bans end. Each dot represents the total number of boats detected in neighboring EEZs, aggregated by nights before/after ban transitions. Day 0 marks the first night following the transition. The x-axis spans 50 nights before and after transitions. Dash lines show local polynomial fits. Sample covers 2012-2017, with neighboring waters defined as EEZs sharing boundaries with Chinese regulatory zones west of 126.5°E. 14

Figure A.12: Boat Density at China's EEZ Boundaries (Excluding China-Vietnam Border)



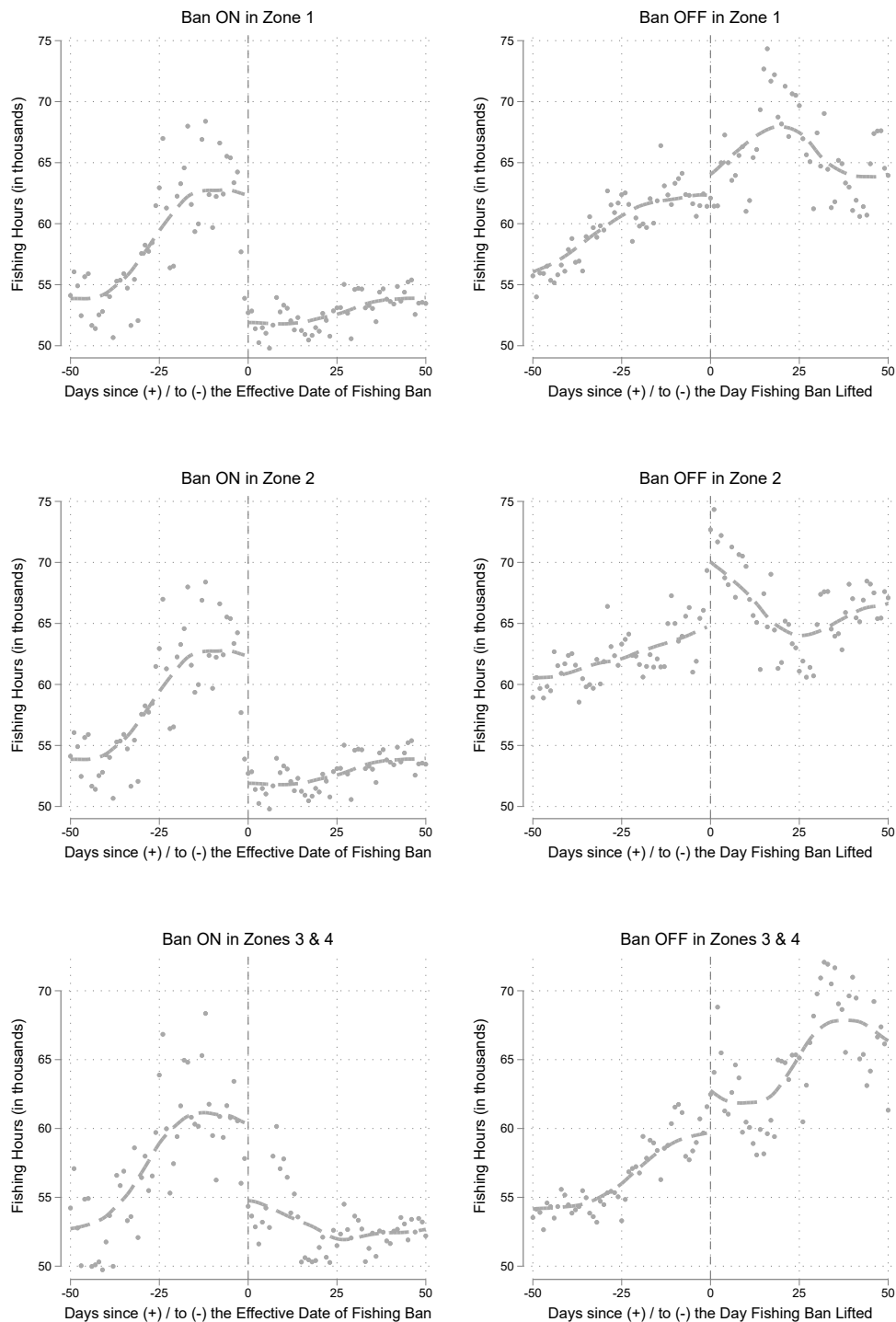
Notes: This figure shows the lack of boat density discontinuities at China's EEZ boundary (excluding China-Vietnam borders) during and outside fishing ban periods. Boat density is measured as detections per km^2 per week, calculated from $5 \text{ km} \times 5 \text{ km}$ grid cells. Red circles show average density during non-ban periods; green hollow diamonds show density during ban periods. Each point represents the average density within a $5 \text{ km} \times 5 \text{ km}$ bin from the EEZ boundary (marked by vertical dashed line at 0), extending to $\pm 100 \text{ km}$. Negative distances indicate areas outside Chinese EEZ; positive distances indicate areas inside. Sample includes all available boat detection data, aggregated separately for ban and non-ban periods. Densities are spatially averaged using grid cell centers for distance calculations.

Figure A.13: Spillover from Zones 3 & 4 to Zones 1 & 2



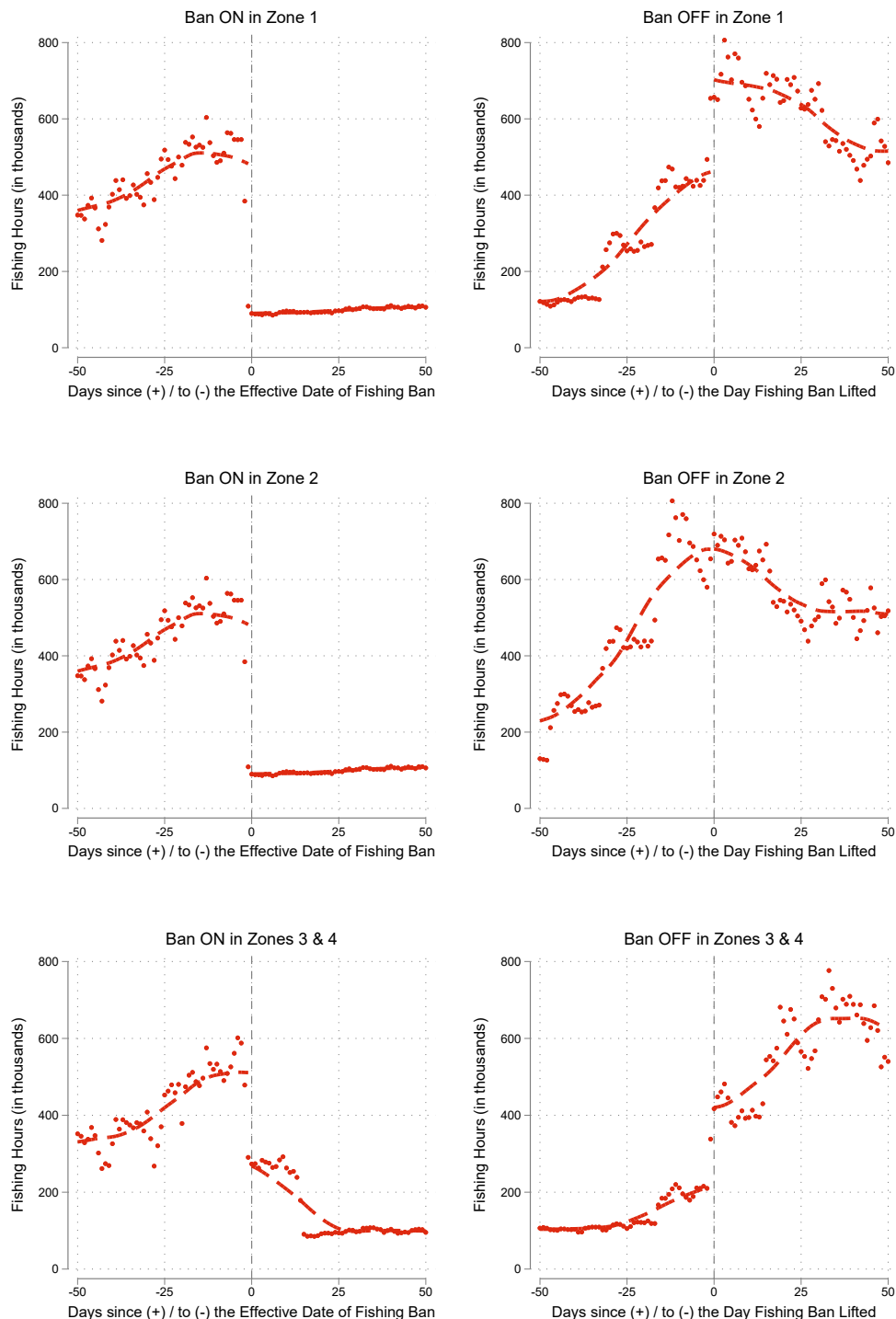
Notes: The RD plots above apply the start and ending dates in Zones 3 & 4 to Zones 1 & 2. The subplots on the left hand side center on the starting of fishing bans in Zones 3 & 4; the subplots on the right hand side center on the lifting of fishing bans in Zones 3 & 4. Rows 1 to 2 represents Zones 1 to 2 respectively. Each dot represents the number of boat detections across the respective zone τ nights since (+) or before (-) the fishing bans became effective (left subplots) or were lifted (right subplots) in Zones 3 & 4. Night 0 is the first night after the fishing bans were lifted in Zones 3 & 4 and the horizontal axis represents τ . The vertical axis represents the nightly number of boat detections in Zone 1 or 2 aggregated over years from 2012 to 2017.

Figure A.14: Fishing Hours of Chinese Fleets outside of Chinese EEZ around the Starts and Ends of Fishing Bans



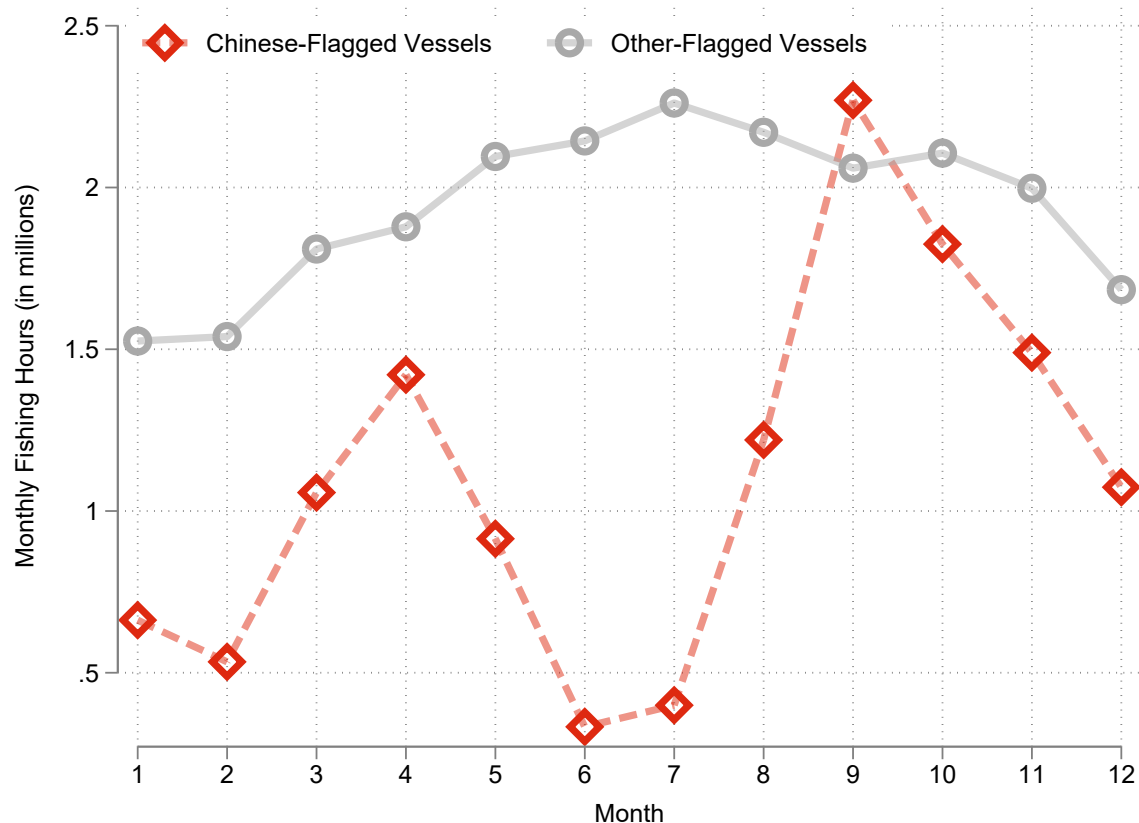
Notes: The RD plots in the figures show the total fishing hours of Chinese fleet outside of Chinese EEZ at the start (left panel) and end (right panel) of fishing bans. The first and second row apply the transition dates of Zones 1 and 2 respectively. The last row applies the dates of Zones 3 and 4, which have the same transition dates.

Figure A.15: Global Fishing Hours of Chinese Fleets around Transitions of Fishing Bans



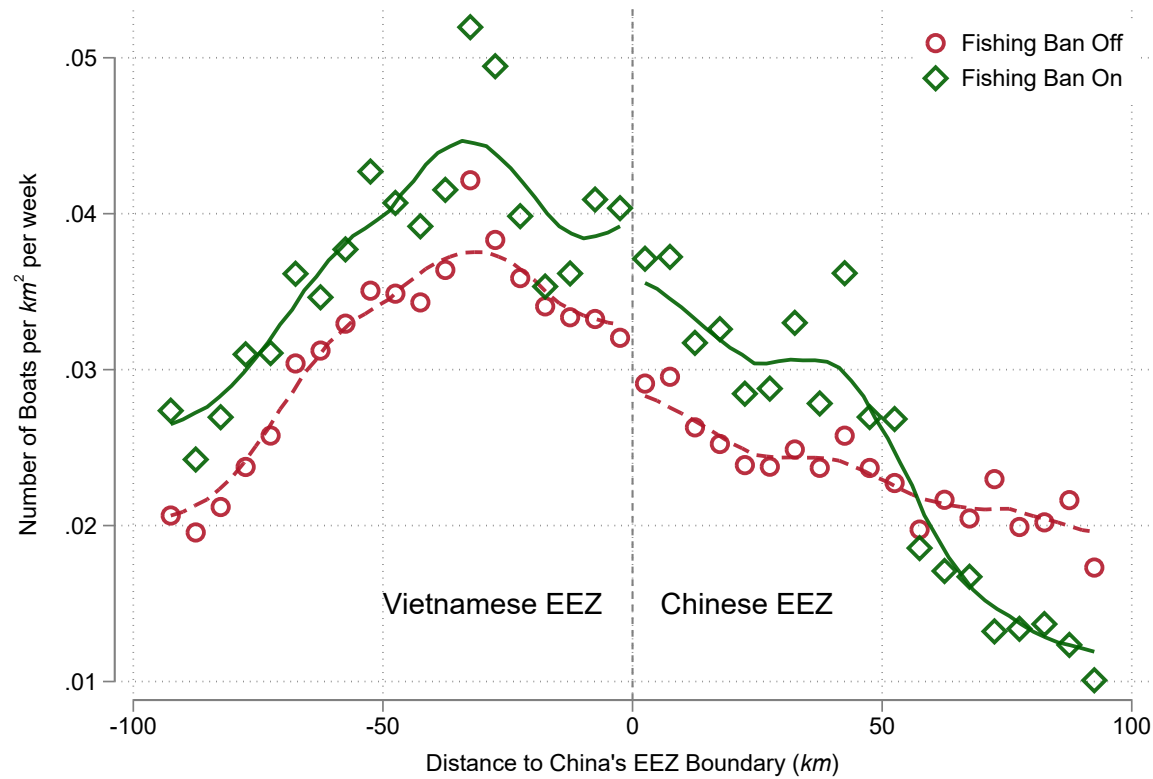
Notes: The RD plots in the figures show the total fishing hours of Chinese fleet globally at the start (left panel) and end (right panel) of fishing bans. The first and second row apply the transition dates of Zones 1 and 2 respectively. The last row applies the dates of Zones 3 and 4, which have the same transition dates.

Figure A.16: Global Fishing Efforts by Month



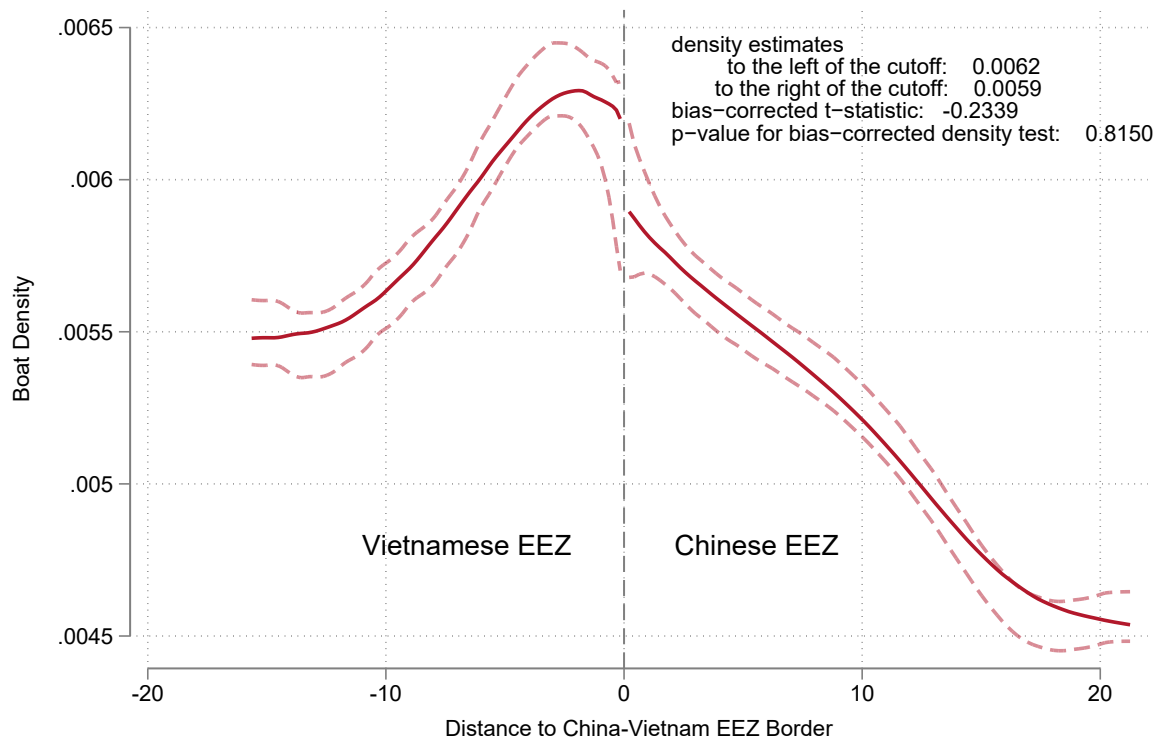
Notes: This figure shows average monthly global fishing effort from 2012-2020, measured in millions of fishing hours, based on Global Fishing Watch AIS data. Red diamonds and dashed line represent Chinese-flagged vessels; gray circles and solid line represent vessels flagged to all other countries. Fishing effort is detected and classified using Global Fishing Watch's neural network algorithm applied to AIS transmissions from fishing vessels. Monthly values represent the sum of fishing hours across all vessels within each flag category. The figure averages across all years in the sample period.

Figure A.17: Boat Density around the China-Vietnam EEZ Boundary



Notes: This figure shows the lack of boat density discontinuities at the China-Vietnam EEZ border during and outside fishing ban periods. Boat density is measured as detections per km^2 per week, calculated from $5 \text{ km} \times 5 \text{ km}$ grid cells. Red circles show average density during non-ban periods; green hollow diamonds show density during ban periods. Each point represents the average density within a 5 km distance bin from the border (marked by vertical dashed line at 0), extending to $\pm 100 \text{ km}$. Negative distances indicate Vietnamese waters; positive distances indicate Chinese waters. Sample includes all available boat detection data, aggregated separately for ban and non-ban periods. Densities are spatially averaged using grid cell centers for distance calculations.

Figure A.18: Spatial Continuity of Boat Density around the China-Vietnam EEZ Boundary



Notes: This figure shows the local polynomial density estimates of boat distribution around the China-Vietnam EEZ border during fishing ban periods. The running variable is the distance to the border (km), with negative values indicating Vietnamese waters and positive values indicating Chinese waters. The solid red line shows the density estimate; dashed lines represent 95% confidence intervals using the Jackknife method with bias corrections. Density estimates are calculated using [Cattaneo et al. \(2020\)](#) simple local polynomial density estimator without pre-binning. Because bias correction is used for the construction of confidence intervals/bands, but not for point estimation, the confidence intervals may not be centered around the point estimates. The point estimates are constructed using local polynomial estimates of order 2, while the bias-corrected confidence intervals are constructed using local polynomial estimates of order 3. Point estimates of densities on either side of the cutoff are reported in the figure.

Table A.1: Fishing Ban and the Number of Boats Detected: RDiT Estimates by Zone

	Ban ON	Ban OFF		
	(1)	(2)	(3)	(4)
Zone 1				
Fishing Ban Effective	-0.869*** (0.246)	-0.695*** (0.173)	-0.810*** (0.206)	-0.510*** (0.117)
Obs.	1330	1330	1261	1261
Zone 2				
Fishing Ban Effective	-1.282*** (0.252)	-1.007*** (0.127)	0.003 (0.317)	0.145 (0.156)
Obs.	1401	1401	1262	1262
Zone 3				
Fishing Ban Effective	-0.878*** (0.320)	-0.783*** (0.220)	-0.567** (0.262)	-0.299 (0.223)
Obs.	900	900	1180	1180
Zone 4				
Fishing Ban Effective	-1.088*** (0.292)	-0.753*** (0.162)	-0.746*** (0.162)	-0.542*** (0.163)
Obs.	1160	1160	1350	1350
Sample	Days before a fishing ban's lifting		Days after a fishing ban becoming effective	
Day of the Year	Quadratic	Quadratic	Quadratic	Quadratic
Day of the Week F.E.	-	X	-	X
Day of the Lunar Month F.E.	-	X	-	X
Share of Cloudy Pixels	-	X	-	X

Notes: This table reports the parametric estimates of fish ban on the log number of boat detections. Panels 1 to 4 from the top represent estimates for Zones 1 to 4 respectively. Each regulatory zone has one fishing ban each year over the sample period from 2012 to 2017. The specifications in Columns (1) and (3) include a quadratic term of the day of the year to control for seasonal effects. The specifications in Columns (2) and (4) additionally include day of the week indicators, day of the lunar month indicators, and the share of cloudy pixels in a regulatory zone in a night. Columns (1) and (2) exploit the discontinuity in time when fishing bans become effective, and therefore drop observations after the fishing bans were lifted in the later part of the year. Columns (3) and (4) exploit the discontinuity in time when fishing bans were lifted by dropping the observations before the fishing bans became effective in the early part of the year. In all columns, "Fishing Ban Effective" is a binary variable that equals one if a fishing ban is in effect on that day and zero otherwise. Newey and West (1986) heteroskedasticity-and-autocorrelation robust standard errors are reported in the parentheses, where the maximum lag of serial correlation is 35 nights. * $p < 0.10$; ** $p < 0.05$; *** $p < 0.01$.

Table A.2: Fishing Ban and the Number of Boats Detected: Nonparametric RDiT Estimates

	Ban ON		Ban OFF	
	(1) # Boats	(2) log(# Boats)	(3) # Boats	(4) log(# Boats)
Aggregate (All Four Zones)				
Ban ON/OFF Switch	-8223.981*** (1091.375)	-1.291*** (0.133)	10701.150*** (2772.387)	0.623*** (0.157)
Obs.	151	151	151	151
Zone 1				
Ban ON/OFF Switch	-1277.873*** (350.677)	-0.959*** (0.292)	866.865 (653.745)	0.171 (0.224)
Obs.	151	151	151	151
Zone 2				
Ban ON/OFF Switch	-2089.284*** (606.819)	-1.901*** (0.263)	4739.264*** (1276.003)	0.875*** (0.239)
Obs.	151	151	151	151
Zone 3				
Ban ON/OFF Switch	-590.585*** (123.537)	-2.674*** (0.407)	910.553 (576.746)	0.465 (0.326)
Obs.	151	151	151	151
Zone 4				
Ban ON/OFF Switch	-4258.144*** (718.816)	-1.171*** (0.147)	3317.123*** (977.563)	0.316 (0.193)
Obs.	151	151	151	151

Notes: This table reports nonparametric RD estimates of fishing ban effects on boat detection counts (Columns 1, 3) and their logs (Columns 2, 4). Columns 1-2 show effects at ban implementation; Columns 3-4 at ban lifting. Panels 2-5 show estimates for Zones 1-4 respectively, while Panel 1 pools all zones. Sample covers 24 fishing bans across 4 zones during 2012-2017. Daily detections are aggregated across years at each temporal distance from ban transitions. Running variable is days from ban implementation (Columns 1-2) or lifting (Columns 3-4). Estimates use bias-corrected local linear estimators following [Calonico et al. \(2014\)](#). Standard errors in parentheses. * $p < 0.10$; ** $p < 0.05$; *** $p < 0.01$.

Table A.3: Fishing Ban and the Number of Boats Detected: Nonparametric Donut Hole RD Estimates

	Ban ON		Ban OFF	
	(1) # Boats	(2) $\log(\# \text{Boats})$	(3) # Boats	(4) $\log(\# \text{Boats})$
Aggregate (All Four Zones)				
Ban ON/OFF Switch	-10257.565*** (786.315)	-1.468*** (0.180)	11702.510 (11708.074)	0.962 (0.805)
Obs.	144	144	144	144
Zone 1				
Ban ON/OFF Switch	-2010.104*** (524.291)	-1.412*** (0.345)	1963.127 (1324.406)	0.878* (0.526)
Obs.	144	144	144	144
Zone 2				
Ban ON/OFF Switch	-3273.804*** (1156.968)	-2.027*** (0.622)	-1303.461 (4952.989)	-0.110 (1.055)
Obs.	144	144	144	144
Zone 3				
Ban ON/OFF Switch	-721.968 (483.771)	-0.378 (0.816)	985.421 (1248.124)	1.079 (1.024)
Obs.	144	144	144	144
Zone 4				
Ban ON/OFF Switch	-4847.571*** (1664.152)	-1.595*** (0.367)	9705.210** (4929.775)	1.339** (0.600)
Obs.	144	144	144	144

Notes: This table reports nonparametric Donut Hole RD estimates of fishing ban effects on boat detection counts (Columns 1, 3) and their logs (Columns 2, 4). Columns 1-2 show effects at ban implementation; Columns 3-4 at ban lifting. Panels 2-5 show estimates for Zones 1-4 respectively, while Panel 1 pools all zones. Sample covers 24 fishing bans across 4 zones during 2012-2017. Daily detections are aggregated across years at each temporal distance from ban transitions. Running variable is days from ban implementation (Columns 1-2) or lifting (Columns 3-4). A 7-day window around the first post-ban night is excluded. Estimates use bias-corrected local linear estimators following [Calonico et al. \(2014\)](#). Standard errors in parentheses. * $p < 0.10$; ** $p < 0.05$; *** $p < 0.01$.

Table A.4: Boat Detections During Fishing Ban by Oceanographic-based Prediction

	Boat Detections (log)			
	(1)	(2)	(3)	(4)
Favorable	0.626*** (0.228)	0.781** (0.311)	0.379 (0.294)	0.454 (0.337)
2nd Half of Ban	0.436*** (0.162)	0.293** (0.125)		
2nd Half of Ban × Favorable	0.324 (0.219)	0.426** (0.199)		
Normalized Duration			0.716** (0.302)	0.347 (0.238)
Normalized Duration × Favorable			0.768* (0.415)	1.074*** (0.390)
Cell Fixed Effects	No	Yes	No	Yes
R ²	0.156	0.446	0.153	0.443
# Obs.	1316	1316	1316	1316

Notes: The dependent variable is the log of the number of boat detections in all columns. Observations are weekly log boat detections within $1^\circ \times 1^\circ$ grid cells during fishing ban periods. "Favorable" is an indicator variable equal to one if out-of-sample boat detections are above the median, and zero otherwise. Predictions are generated from a LASSO regression, as in Figure A.10. "Second Half of Ban" is an indicator variable equal to one if the week falls within the second half of a fishing ban, and zero otherwise. "Normalized Duration" represents the normalized fishing ban duration, corresponding to the horizontal axis in Figure A.10. Columns (2) and (4) include $1^\circ \times 1^\circ$ grid cell fixed effects. Robust standard errors, clustered by $1^\circ \times 1^\circ$ grid cell, are in parentheses.

* $p < 0.10$; ** $p < 0.05$; *** $p < 0.01$.

Table A.5: RDiT Estimates on Boats Detected by Fishing Favorability

	Ban ON		Ban OFF	
	(1)	(2)	(3)	(4)
Fishing Ban Effective	-1.515*** (0.145)	-0.524*** (0.163)	-0.922*** (0.134)	-0.502*** (0.146)
Obs.	4047	4265	4290	4608
Sample Cells				
Fishing Favorability	Low	High	Low	High

Notes: This table reports parametric estimates of fishing ban effects on the log number of boat detections. All specifications include a quadratic term for day of the year to control for seasonal effects, day of the week indicators, day of the lunar month indicators, and the share of cloudy pixels in a regulatory zone per night. Columns (1) and (2) exploit the discontinuity in time when fishing bans become effective, dropping observations after the bans were lifted in the later part of the year. Columns (3) and (4) exploit the discontinuity when fishing bans were lifted, dropping observations before the bans became effective in the early part of the year. In all columns, “Fishing Ban Effective” is a binary variable that equals one if a fishing ban is in effect on that day and zero otherwise. All specifications include fixed effects for regulatory zones. Before aggregating to zone-level time series, $1^\circ \times 1^\circ$ grid cells are split into two subsamples based on their above- or below-median out-of-sample average predicted boat detections during fishing bans. The out-of-sample predictions are obtained from the same LASSO regression that produces Figure A.10. Unlike Table A.4, this sample split is based on cell averages and is therefore time-invariant. Columns (1) and (3) use cells with below median fishing favorability, while Columns (2) and (4) use cells with above median fishing favorability. Newey and West (1986) heteroskedasticity-and-autocorrelation robust standard errors are reported in parentheses, with a maximum lag of serial correlation of 35 nights.

* $p < 0.10$; ** $p < 0.05$; *** $p < 0.01$.

Table A.6: Fishing Ban and the Number of Boats Detected in Neighboring EEZs: Nonparametric RD Estimates

	Ban ON		Ban OFF	
	(1) # Boats	(2) log(# Boats)	(3) # Boats	(4) log(# Boats)
Aggregate (Neighbors of All Four Zones)				
Ban ON/OFF Switch	-1791.638** (753.250)	-0.201* (0.112)	2501.351* (1292.850)	0.238* (0.127)
Obs.	151	151	151	151
Zone 1 Neighbors				
Ban ON/OFF Switch	-392.609*** (111.890)	-0.372*** (0.110)	280.158 (361.882)	0.059 (0.217)
Obs.	151	151	151	151
Zone 2 Neighbors				
Ban ON/OFF Switch	-553.975*** (189.224)	-0.532*** (0.152)	470.575 (696.185)	0.182 (0.258)
Obs.	151	151	151	151
Zone 3 Neighbors				
Ban ON/OFF Switch	-628.880*** (231.152)	-1.112*** (0.319)	336.345 (378.163)	0.093 (0.328)
Obs.	151	151	151	151
Zone 4 Neighbors				
Ban ON/OFF Switch	-54.245 (720.103)	-0.042 (0.151)	1919.781*** (557.453)	0.616*** (0.163)
Obs.	151	151	151	151

Notes: This table reports nonparametric RD estimates of Chinese fishing ban spillover effects on boat detections in neighboring EEZs. Columns 1-2 show effects at ban implementation; Columns 3-4 report effects at ban lifting, using counts and log counts respectively. Panels 2-5 show estimates for areas adjacent to Zones 1-4, while Panel 1 pools all neighboring areas. Sample covers 24 fishing bans across 4 zones during 2012-2017. Daily detections are aggregated across years at each temporal distance from ban transitions. Running variable is days from ban implementation (Columns 1-2) or lifting (Columns 3-4). Estimates use bias-corrected local linear estimators following [Calonico et al. \(2014\)](#). Standard errors in parentheses.* $p < 0.10$; ** $p < 0.05$; *** $p < 0.01$.

B Appendix B: Data Description

B.1 VIIRS Boat Detection Data

The primary dataset used in this paper is the VIIRS Boat Detection (VBD) data, provided by the National Oceanic and Atmospheric Administration (NOAA). The VBD project, jointly sponsored by NOAA and the U.S. Agency for International Development, utilizes remote sensing imagery from the Suomi National Polar-orbiting Partnership satellite.

NOAA, in collaboration with the National Atmospheric Administration, developed the Joint Polar Satellite System (JPSS), a next-generation polar-orbiting operational environmental satellite program in the U.S. Launched in 2011, JPSS is intended to replace the U.S. Air Force's Defense Meteorological Satellite Program (DMSP), with the Suomi NPP as the program's first satellite. The second satellite, JPSS-1, was launched in November 2017.

Most prior economic studies using remote sensing data have relied on imagery from the DMSP-OLS program.⁵

The VIIRS Boat Detection data are derived from images captured by the Visible Infrared Imaging Radiometer Suite (VIIRS), the primary imaging instrument on the Suomi NPP satellite. Compared to the imaging sensors in the DMSP Operational Linescan System (DMSP-OLS), VIIRS provides superior remote sensing imagery, offering higher spatial resolution and an enhanced ability to detect faint light sources. Specifically, nighttime DMSP-OLS pixels cover a $5 \text{ km} \times 5 \text{ km}$ area, while the VIIRS Day/Night Band (DNB) sensor captures a finer $742 \text{ m} \times 742 \text{ m}$ footprint. The low-light imaging detection limit is approximately $5 \times 10^{-10} \text{ Watts/cm}^2/\text{sr}$ for DMSP-OLS, compared to $2 \times 10^{-11} \text{ Watts/cm}^2/\text{sr}$ for VIIRS. In summary, the VIIRS DNB offers roughly 45 times finer spatial resolution and is 25 times more sensitive in low-light imaging than DMSP-OLS (Elvidge et al., 2013).

In addition, as its name suggests, VIIRS can capture both imagery and radiometric measurements across the visible and infrared bands of the electromagnetic spectrum. This capability allows for distinguishing light from human activities, such as fishing vessels and LED lighting, from other sources like gas flares at oil fields or explosions in conflict zones (Elvidge et al., 2015b).

Since 2000, fishery agencies in Japan, Korea, Thailand, and Peru have received per-

⁵See Donaldson and Storeygard (2016) for a review of this literature.

mission to use DMSP-OLS data for fishery management, albeit with a minimum three-hour delay. However, DMSP-OLS's limited capacity for low-light detection at fine spatial resolutions, coupled with the lack of automated boat detection algorithms, has restricted its utility for fishery management applications. The VIIRS Boat Detection project has significantly enhanced satellite imagery's role in fishery management by developing an automated boat identification system using VIIRS DNB images, which rely on sensors adapted to a broad wavelength spectrum.

In a nutshell, the VBD algorithm detects spikes in illumination from offshore areas in the DNB images while controlling background noise radiance caused by moonlight. It also filters out recurring light sources (such as features on land) and energetic particles in the upper atmosphere (ionosphere) that can affect electromagnetic sensors. The algorithm further classifies boat detections as either strong or weak by comparing the spikes to neighboring pixels. Additionally, it uses the spectral characteristics of a spike to identify and label gas flares, such as those from offshore drilling stations. For more in-depth information about the algorithms, please refer to [Elvidge et al. \(2015a\)](#), which also includes a validation study demonstrating that the algorithm correctly identified 99.3% of the reference pixels. These reference pixels were chosen from a set of 594 boats visually identified by an analyst and an additional 245 pixels that were not initially identified by the analyst.

Given that the boat detection is a product of remote sensing imagery, the ability to detect boats is considerably affected by the prevailing weather in a location. Although the algorithm adopted a sharpness index to rate the sharpness of features and identify detection that is affected by clouds, dense clouds, rains, and storms limit the ability for the remote sensing to capture night light and hence detect light emitted by boats. Moreover, the sensors and algorithm are most capable of detecting offshore boats at night with new moon, where the oceans are less lit by moonlight. In full moon nights, the algorithm could have false identifications of boats due to the brightness variations in clouds.

However, despite its limitations, the VBD data offers a unique dataset of offshore boats at a high frequency across an extensive spatial scale. The VBD data is available for most Exclusive Economic Zones (EEZs) in Asia, Oceania, North America, and select European countries. Notably, the VBD data covers all of China and its neighboring countries' EEZs. Since the Suomi NPP scans the same location twice, once around noon and again around 1:30 AM local time, the VBD data provides daily (nightly) boat identifications at a fine spatial resolution across a vast geographic area.

The VBD data analyzed here cover the period from April 2, 2012, to December 31, 2017. The sample includes both strong and weak boat detections while excluding blurry detections, gas flares, glows, recurring lights, and offshore platforms. Figure 1 displays two heatmaps illustrating the spatial density of aggregated boat detections over the sample period. Both maps cover the same geographic region, encompassing China's EEZ and adjacent waters. The left panel employs a spatial resolution of one degree latitude and longitude, equivalent to approximately 110 kilometers north-south and 100 kilometers east-west.⁶

As shown in the left subplot of Figure 1, marine areas near the shore are generally brighter than international waters or distant EEZs. The brightest regions, indicating the densest concentrations of detected boats, are near the shores of Beijing, Tianjin, Shanghai, Hong Kong, and Guangzhou—China's largest cities. Each hexagonal cell in the heatmap covers approximately 7,100 km². In the areas with the highest boat density, there are up to 200,000 detections per cell, equating to nearly 28 detections per square kilometer over 4.75 years.

The right subplot of Figure 1 presents a similar heatmap with a finer spatial resolution. Here, each hexagon spans 0.1 degrees of latitude and longitude, covering an area of approximately 71 km². Densest areas record up to 10,000 detections per cell, or close to 140 detections per square kilometer over 4.75 years. Additionally, several bright spots are visible near the Shandong Peninsula, which is surrounded by the Yellow Sea in eastern China around N 37°, and near the Liaodong Peninsula, also bordered by the Yellow Sea in northern China around N 40°.

Overall, coastal areas exhibit higher densities of boat detections, consistent with previous studies using Automatic Identification System (AIS) data to map fishing activity distributions in Chinese waters (Yan et al., 2022).

Outside China's EEZ, significant boat detection activity is visible near the southern Korean Peninsula, particularly around Jeju Island, the largest island of South Korea. The marine area off Vietnam's coast also shows a notable band of detections, aligning with the known overfishing pressures in this region (U.N. Food and Agriculture Organization, 2014). Figure 1 highlights substantial spatial variation in fishing intensities, with certain regions clearly serving as primary fishing grounds.

⁶1 km is approximately 0.621 miles, and 1 mile is approximately 1.609 km; 1 nautical mile is 1.852 km.

B.2 Cloud Cover

Since cloud cover limits a satellite remote sensor's ability to detect light and, consequently, boats at night, accounting for cloud cover in an ocean area allows for more accurate estimates of nighttime boat detection. I obtained global cloud cover images from the Earth Observation Group at the Payne Institute for Public Policy, Colorado School of Mines.⁷ The nightly cloud cover data, derived from the VIIRS cloud mask, have a spatial resolution of 15 arc seconds, or approximately 500 meters at the Equator. These data indicate whether a given pixel is cloud-covered. Together with the nightly VIIRS DNB imagery mosaic, the cloud cover mask served as input for the VIIRS Boat Detection (VBD) algorithms and outputs discussed in the previous section. For further details on VIIRS nightlight products, see Elvidge et al. (2013, 2017).

I aggregate pixels within a regulatory zone in China's EEZ to calculate the proportion of pixels covered by clouds on a given night when the Suomi NPP satellite scans a geographic area.

B.3 NASA Ocean Color

Oceanographic conditions have been shown to influence the economic returns of marine fishing (see, e.g., Flückiger and Ludwig, 2015; Axbard, 2016 and references therein). Satellite-based remote sensing offers opportunities to monitor global oceanographic conditions with fine spatial resolution and high temporal frequency. NASA's Ocean Biology Processing Group collects and processes satellite imagery, providing these data products through the Ocean Color platform.

The color of the ocean is influenced by the interaction of sunlight with microscopic particles within the water, including phytoplankton, minerals, and organic matter. The absorption and scattering of different light wavelengths by these materials determine the ocean's perceived color.

Phytoplankton, a crucial component of marine ecosystems, form the base of the oceanic food web and are the primary food source for small pelagic fish essential to human diets. These microscopic, single-celled plants use chlorophyll-a for photosynthesis, similar to terrestrial plants. Consequently, productive waters rich in phytoplankton generally appear green due to chlorophyll-a, while less productive waters appear blue.

⁷<https://payneinstitute.mines.edu/eog/>

Scientists can estimate phytoplankton concentrations by measuring chlorophyll-a levels via satellite data. This information offers insights into the distribution and abundance of phytoplankton, providing a valuable indicator of marine ecosystem health and productivity.

I obtained data on the concentration of the photosynthetic pigment chlorophyll-a in near-surface ocean water from NASA's Ocean Color.⁸ Chlorophyll-a concentration, measured in mg/m^3 , is calculated using empirical relationships between field-measured chlorophyll-a levels and spectral remote sensing reflectances (Rrs). This calculation requires three or more spectral bands spanning the 440–670 nm range, which the VIIRS sensor satisfies (Hu et al., 2019). Chlorophyll-a concentration data are available at a daily frequency throughout the sample period, with a spatial resolution of 9 km × 9 km.

I also obtained sea surface temperature data from NASA's Ocean Color. These measurements, derived similarly from VIIRS imagery, are available at the same temporal frequency and spatial resolution. These two variables provide valuable information on the biological productivity of marine areas.

B.4 AIS-based Measures of Fishing Efforts

To measure apparent fishing effort, Global Fishing Watch uses data from the Automatic Identification System (AIS)—a vessel tracking system originally designed for collision avoidance—and applies machine learning techniques to detect fishing vessels and activities.

Specifically, Kroodsma et al. (2018) trained two convolutional neural networks (CNNs). One CNN classifies fishing vessels by learning the characteristics of fishing and non-fishing vessels from official fleet registries. The other CNN detects fishing activities by analyzing 22 billion global AIS positions from 2012 to 2016. AIS devices broadcast a ship's identity, position, speed, and turning angle every few seconds. This information is instrumental in inferring fishing activities; for example, trawlers typically travel at much lower speeds while fishing compared to when they are in transit, resulting in a bimodal speed distribution for trawlers (Yan et al., 2022).

Using updated AIS algorithms, neural network models, and a comprehensive vessel registry database, Global Fishing Watch provides a dataset on global marine fishing effort from 2012 to 2020. This dataset, which I obtained from Global Fishing Watch, is

⁸<https://oceancolor.gsfc.nasa.gov/>

available at the vessel level with a spatial resolution of 0.1 degrees. It monitors over 100,000 unique fishing vessels, with approximately 70,000 active annually. I observe the number of active fishing vessels in each 0.1-degree geographic grid cell daily, along with their fishing hours within these cells.

This dataset offers valuable insights into the intensity of fishing activities that may not be fully captured by nighttime boat detections alone. Moreover, since the dataset includes the registration country of each vessel, it enables an analysis of fishing activities within an EEZ and the specific countries involved.

B.5 AIS-disabling Events

A limitation of AIS data is that AIS devices can be turned off to evade monitoring, particularly during potentially illegal fishing activities. To examine the extent to which AIS-disabling behaviors might impact my previous AIS-based analysis, I obtained a dataset of AIS-disabling events from Global Fishing Watch.

Using machine learning techniques, [Welch et al. \(2022\)](#) derived data on AIS (Automatic Identification System) disabling events from Global Fishing Watch's AIS dataset, which includes over 3.7 billion AIS messages from fishing vessels between 2017 and 2019. They developed a rule-based classification model to identify gaps in AIS transmissions likely caused by intentional disabling.

The resulting dataset, limited to waters more than 50 nautical miles from shore to minimize noise from technical issues, revealed over 55,000 suspected disabling events. Importantly, this dataset captures disabling events only from vessels that broadcast AIS at some point, representing a subset of global fishing activity. The dataset provides details for each suspected disabling event, including location, time, duration, and vessel characteristics (flag state, gear type, length, and tonnage).

B.6 Import Price of Frozen Fish

Trade statistics on China's seafood imports are obtained from the United Nations Comtrade platform. Since China does not report monthly import statistics to Comtrade, I construct monthly import prices using export records from China's major trading partners. Specifically, I access data via Comtrade's public API to collect export values and volumes (weight) reported by the top 20 seafood exporters to China, identified based on annual trade flows. The sample covers 2010-2017, with Russia, the U.S., Canada, Norway, and New Zealand comprising the top five exporters.

The average monthly import price is calculated by aggregating total export value across these major trading partners and dividing by total exported weight. This approach leverages the mirror statistics principle in international trade data, where one country's exports should match its trading partner's imports. While this method may not capture all of China's seafood imports, it covers the majority of trade flows given the concentrated nature of global seafood exports.

B.7 EEZ Boundaries

I obtained Geographic Information Systems (GIS) data from the Marine Regions organization (<https://www.marineregions.org/>), using the Version 8 World EEZ Boundaries dataset published in 2014.

The Paracel Islands in the South China Sea are controlled and claimed by China, but their sovereignty is disputed by the governments of Vietnam and Taiwan. The Spratly Islands are claimed by China, Indonesia, Malaysia, the Philippines, Taiwan, and Vietnam. All of these governments, except Indonesia, also control parts of the Spratly Islands. China's maritime claims in the South China Sea further conflict with those of Brunei. Additionally, China, Taiwan, and Japan claim uninhabited islands respectively named Diaoyudao Islands, Diaoyutai Islands, and Senkaku Islands. These disputed islands are located to the northeast of Taiwan and to the west of Okinawa Island.

Due to the complications arising from these sovereignty disputes, I have excluded the EEZs claimed by China that are derived from the sovereignty of these disputed islands in my analysis in this paper. Moreover, I have also excluded the EEZs claimed by China that are derived from islands controlled by the Taiwan authorities. Throughout this paper, I refer to Taiwan as a geographic area or its government without implying any particular legal status. Similarly, I refer to China as the authority of the People's Republic of China (P.R.C.) or as a geographic area where the P.R.C. maintains effective and undisputed control.